Jet vectoring using synthetic jets

By B. L. SMITH[1]† AND A. GLEZER[2]

[1]Los Alamos National Laboratory, Los Alamos, NM 87545, USA

[2]Woodruff School of Mechanical Engineering, Georgia Institute of Technology,
Atlanta, GA 30332-0405, USA

The interaction between a conventional rectangular (primary) air jet and a co-flowing synthetic jet is investigated experimentally. The nozzles of both jets have the same long dimension but the aspect ratio of the synthetic jet orifice is 25 times larger. Detailed particle image velocimetry (PIV) measurements of the flow in the midspan plane show that primary jet fluid is directed into the synthetic jet orifice and the interaction between the jets leads to the formation of a closed recirculating flow domain. The concomitant formation of a low-pressure region between the jets results in deflection of the primary jet toward the actuator jet despite the absence of an extended control surface (e.g. a diffuser or collar) and is balanced by a force on the primary jet conduit. For a given synthetic jet strength and primary jet speed, the vectoring force depends mainly on the volume flow rate of primary jet fluid that is diverted into the synthetic jet actuator. This flow rate is regulated by restricting the flow of entrained ambient fluid using a small streamwise extension of the synthetic jet orifice that scales with the orifice width. The response of the primary jet to the imposed vectoring is investigated using stepped modulation of the driving signal. The characteristic vectoring time and vectoring angle decrease monotonically with primary jet speed.

1. Introduction

The modification of the global flow characteristics of conventional jets with the objective of affecting the flow direction (e.g. Strykowski, Krothapalli & Forliti 1996) and its cross-stream spreading and mixing (e.g. Wiltse & Glezer 1998), has been of considerable interest because of its relevance to a number of applications including thrust vectoring, the reduction of thermal signature and noise abatement.

Methods of jet vectoring can be divided into two distinct groups, namely, approaches that rely primarily on extended surfaces, and approaches that are based on fluidic actuation. In the former, the flow direction of a planar jet can be substantially altered either by exploiting the adherence of the jet to a curved surface that is a smooth extension of its nozzle, or by the reattachment of a separated jet to an adjacent solid surface. As discussed by Newman (1961), a two-dimensional wall jet issuing along the surface of a circular cylinder can remain attached to the surface within a finite domain downstream of the jet exit plane where the static pressure along the surface is lower than the ambient pressure. As a result of the increase in jet width and the decrease in its azimuthal velocity (owing to entrainment), the streamwise

† Present address: Department of Mechanical & Aerospace Engineering, Utah State University, Logan, UT 84322-4130, USA

static pressure approaches the ambient pressure, ultimately resulting in boundary-layer separation. Experiments demonstrated that for jet slot width to cylinder radius ratio $b/a = 0.02$ and jet Reynolds number above $15\,000$, the jet remains attached to the surface over azimuthal angles that exceed $180°$ (the separation angle increases with Reynolds number). Newman also noted that a second mechanism by which the flow direction of a plane jet can be altered is the attachment of a separated jet to an adjacent solid surface that extends to the edge of the nozzle. This attachment is induced by the formation of a low-pressure region between the jet and the surface owing to entrainment and is known as the Coanda effect. Depending on the surface angle relative to the jet centreline, the separated jet forms a recirculating flow bubble before it attaches to and flows along the surface. The circulating flow within the separation bubble is a balance between entrainment into the jet and the return flow upstream of the reattachment zone.

Vectoring of primary jets by interaction with (typically) smaller scale secondary control jets of the same fluid within an enclosed cavity has been studied since the late 1950s in connection with the development of fluidic actuators. These actuators perform a variety of 'analog' (e.g. proportional fluidic amplifier) and 'digital' (e.g. flip-flop) throttling and control functions in flow systems without moving mechanical parts (Joyce 1983). In the 'analog' actuator, the volume flow rate fraction of two opposite control jets leads to a proportional change in the volume flow rate of the primary stream out of one of two output ports. The 'digital' actuator is a bistable flow device in which the control jets and Coanda effect are used to direct most of the primary stream into one of two output ports. Although fluidic technology has been primarily restricted to enclosed cavities, some of these devices have also been used in free shear flows. Viets (1975) induced spontaneous oscillations in a free rectangular jet by exploiting the concept of a flip-flop actuator. More recently, Raman & Cornelius (1995) used two such jets to impose time-harmonic oscillations in a larger jet by direct impingement. The control jets were placed on opposite sides of the primary jet and could be operated in phase or out of phase with each other.

The attachment of separated jet flows to adjacent solid surfaces can be significantly enhanced by time-invariant suction. Of particular note is jet vectoring that is achieved by using low-volume suction to induce countercurrent flow between the edge of a rectangular Mach 2 primary jet and an external collar (Strykowski *et al.* 1996; Flamm 1998). The countercurrent flow leads to increased mixing (which, as asserted by the authors, is larger than in co-flowing streams having the same velocity difference) that in turn results in low-pressure regions near the collar. The primary jet is deflected towards the low-pressure region at angles as large as $16°$ and flows along the external collar.

Partial attachment of the jet column to an adjacent solid boundary can also be effected by exploiting the receptivity of the shear layer of free jets to relatively small controlled external perturbations near the jet exit plane (e.g. Crow & Champagne 1971; Cohen & Wygnanski 1987*a,b*) which can lead to a substantial increase in the entrainment of ambient fluid into the jet. Koch (1990) used eight individually controlled azimuthal jet actuators to stabilize the flapping motion of a primary circular continuous jet in a transitory stall within a circular diffuser mounted at the downstream edge of the primary jet nozzle. The secondary control jets were switched on and off using fast solenoid valves. Two types of actuation were considered, based on radial (transverse) or tangential (wall-jet) blowing. Whereas the former resulted in pushing of the primary jet away from the control jet, the latter mode of actuation exploited a Coanda-like effect induced by the wall jet (cf. Newman 1961). In a more

recent experiment, Pack & Seifert (1999) used an array of eight synthetic (zero-net-mass flux) jets to vector and modify the cross-section of an axisymmetric continuous jet. Similar to the concept introduced by Koch, the primary jet exit was fitted with a wide-angle conical diffuser whose length was of the order of the primary jet diameter. The time-periodic disturbances introduced by the synthetic jet actuators that are discussed in more detail below, cause an increase in entrainment into the forced segments of the jet shear layer which in turn lowers the local pressure between the jet and the wall of the diffuser, resulting in the deflection of the jet toward the wall. Although the frequency of the Kelvin–Helmholtz instability of the unforced primary jet was not reported, the invariance of the results with the dimensionless forcing frequency suggests that it was well above the unstable frequency band of the jet.

The vectoring approaches described above rely on the presence of an extended surface downstream from the primary jet exit plane that also supports the vectoring force. In contrast, aerodynamic vectoring approaches that are based on the inter-action between adjacent fluid streams and do not require extended surfaces were demonstrated by Hammond & Redekopp (1997) in a shear layer between parallel streams of different speeds and by Smith & Glezer (1994) in a rectangular jet. In a numerical investigation, Hammond & Redekopp (1997) used suction at the down-stream end of the flow partition in a plane shear layer to effect vectoring toward the high-speed stream. For sufficiently large suction volume flow rate (suction speed of the order of 20%–40% of the free-stream velocity), the global (absolute) instability of the flow partition wake is suppressed and the low-speed fluid is vectored towards the high-speed side. These authors also reported that the direction and extent of the vectoring can be altered by modifying the symmetry of the suction flow, such that the shear layer is vectored toward the side from which the bulk of the suction flow is entrained.

The interaction between a primary conventional jet and adjacent zero net mass flux (synthetic) control jets in the absence of extended control surfaces was investigated by Smith & Glezer (1994, 1997). The control jets have the unique property that they are synthesized from the working fluid of the flow system in which they are deployed and thus, in contrast to conventional continuous jets (e.g. Gutmark & Wygnanski 1976) or pulsed jets (Bremhorst & Hollis 1990), synthetic jets can transfer linear momentum to the flow without net mass injection across the flow boundary. Synthetic jet actuation is an attractive tool for flow control applications because it provides a localized combination of alternating blowing and suction (through the same flow orifice) while eliminating the need for an additional fluid source and extraneous pumping and piping. However, this form of actuation clearly requires the development of actuators that can deliver the oscillatory flow at a desired frequency and amplitude within the geometrical constraints of a given flow apparatus.

The flow field of a two-dimensional synthetic jet that is formed normal to an orifice in a flat plate was studied in detail by Smith & Glezer (1997, 1998) and Smith (1999). As shown schematically in figure 1, these jets are synthesized by the time-periodic formation and subsequent advection of a train of counter-rotating vortex pairs. The vortices are formed at the edge of the jet orifice by the time-periodic motion of a diaphragm bounding a sealed cavity underneath the orifice plate. Although, in the far field, synthetic jets are globally similar to conventional continuous jets (e.g. in terms of cross-stream spreading and the decay of centreline velocity), these flows are substantially different in the near field (Smith & Swift 2001). In particular, owing to the suction flow, the time-averaged static pressure near the exit plane of a synthetic
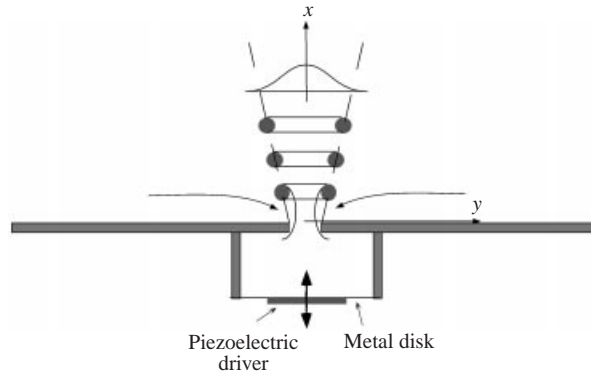
FIGURE 1. Schematic diagram of a synthetic jet.

jet is lower than the ambient pressure and both the streamwise and cross-stream velocity components reverse their direction during the actuation cycle.

The present work is an experimental investigation of the interaction between a primary conventional rectangular jet and smaller-scale high-aspect-ratio synthetic jets. Earlier investigations (Smith & Glezer 1997) showed that entrainment of primary jet fluid by an adjacent synthetic jet leads to alteration of the static pressure near the flow boundary and results in deflection of the primary jet toward the synthetic jet. The present investigation focuses on the structure of the nominally two-dimensional interaction domain between the primary and control jets, and on the flow mechanisms that result in the vectoring of the primary flow. Attention is restricted to the flow domain near the exit plane of the primary jet where spanwise variations of the vectored flow (not including edge effects) are reasonably small. An important aspect of this work is the identification, characterization, and scaling of the flow parameters that significantly affect the vectoring. The experimental apparatus is described in § 2 which also includes a discussion of the synthetic jet actuators and the parameters that affect their performance. Some near-field flow features of synthetic jets that are relevant to their interaction with other flows are described in § 3. As shown, an important feature of the flow field is the ability to regulate spatially the entrainment into the synthetic jet cavity by subtle changes of the orifice geometry. Sections 4 and 5 discuss the interaction between the jets in detail, and characterize its dependence on the flow parameters that are identified in the previous sections. Scaling of the vectoring force is presented at the end of § 5. The actuation discussed in §§ 4 and 5 is applied at frequencies that are typically higher than the 'natural' unstable frequencies of the base flow and, therefore, the vectoring of the primary jet may be thought of as quasi-steady. The response of the vectored jet to time-varying actuation is discussed in § 6.

2. Experimental apparatus and procedure

2.1. *The jet facility*

The primary (continuous) air jet emanates from a 71 cm long rectangular aluminium conduit having a cross-section measuring $12.7\,\text{mm} \times 76.2\,\text{mm}$. The air jet facility (except the present nozzle conduit) is described in detail in Wiltse & Glezer (1993). The rectangular conduit is centrally mounted on the downstream endplate of a cylindrical plenum tube and its downstream edge is flush with (and normal to) a flat
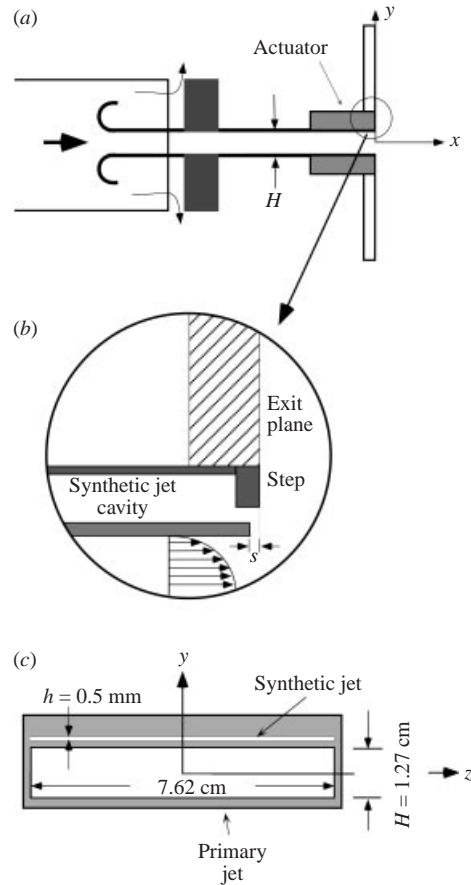
FIGURE 2. (*a*) Schematic diagram of synthetic jet in the (x, y)-plane. (*b*) Close-up of the exit plane. (*c*) Schematic of the exit in the (y, z)-plane.

plate that forms the exit plane, as shown in figure 2(*a*). No contraction is used, and secondary flows at the inlet and along the corners of the conduit are minimized by azimuthal bleeding through a gap along the perimeter of the plenum that is adjusted to provide a nominally uniform streamwise velocity distribution upstream of the inlet to the jet conduit. In the present experiments, the mean centreline velocity U_{cl} is varied between 4 and 33 m s^{-1}, which is the practical range of the blower. The flow in the conduit becomes turbulent when the centreline velocity is approximately 8 m s^{-1} and the conduit Reynolds number is $Re_H = U_{ave}H/v = 5.83 \times 10^3$, where U_{ave} is the cross-stream average velocity, H is the primary jet height, and v is the kinematic viscosity. A co-flowing rectangular synthetic jet having an orifice measuring 0.51 mm × 76.2 mm is mounted in the exit plane on top of the primary jet and along the long side of the jet conduit as shown in figure 2. The conduit wall that separates the synthetic jet from the primary jet is 1.8 mm thick.

In some of the present experiments, the top edge of the synthetic jet orifice is uniformly extended in the streamwise direction (figure 2b). The extension is referred to below as a 'step', and its downstream length s is at least an order of magnitude smaller than the primary jet height. As discussed below, the purpose of the step is to alter the symmetry of the entrainment flow of the synthetic jet. It is important to note that in contrast to some of the vectoring schemes discussed above (e.g. Koch 1990;
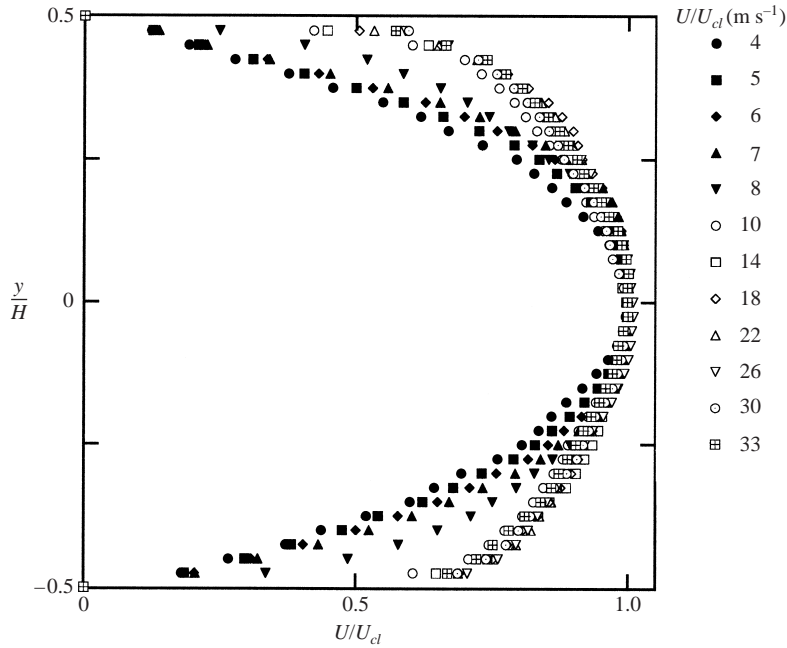
FIGURE 3. Cross-stream distributions of the streamwise velocity component of the unforced primary jet.

Strykowski *et al.* 1996; Pack & Seifert 1999), the present approach does not rely on the presence of a Coanda surface in the form of nozzle extensions that scale with the primary jet.

The primary jet conduit is fitted with ten pressure taps along the spanwise centre-lines of the top and bottom walls. The taps are equally spaced between $x/H = -0.3$ and -2.1. Sections of the conduit sidewalls upstream of the exit plane are constructed of transparent plastic plates to allow for optical access (e.g. particle image velocimetry, PIV). The primary jet is driven by an axial blower powered by a d.c. motor equipped with a feedback controller that maintains a preset angular velocity to within 1%.

Cross-stream distributions of the time-averaged streamwise velocity $U(y)$ measured using PIV at the exit plane of the primary jet for a number of jet speeds are plotted in figure 3 in the usual similarity variables and appear to be symmetric about the jet centreline. Although the wall boundary layers apparently reach the centre of the duct, the flow in the duct is not fully developed. The duct length was selected to be long enough so that the flow at the exit is decoupled from inlet non-uniformities at the plenum but short enough to prevent spanwise non-uniformities as a result of the evolution of secondary flows in the corners. Measurements of spanwise velocity distributions (not shown) indicate that the flow inside the conduit is uniform outside of the boundary layers on the spanwise edges of the duct. The velocity distributions form two distinct groups depending on whether the flow in the conduit is laminar (i.e. $U_{cl} < 8\,\mathrm{m\,s^{-1}}$) or turbulent. The latter results in typical velocity distributions having lower cross-stream gradients in the central part of the conduit. The respective average streamwise velocities within the conduit for laminar and turbulent flows are $U_{ave} = 0.72U_{cl}$ and $0.86U_{cl}$ (the corresponding average velocities in fully developed laminar and turbulent two-dimensional channel flows are $0.67U_{cl}$ and $0.8U_{cl}$) and the conduit Reynolds number Re_H varies between 2270 and 24000.

2.2. *The synthetic jet actuator*

The evolution of a high-aspect ratio rectangular synthetic (zero net mass flux) jet similar to the baseline configuration (i.e. $s = 0$) of the actuator jet in the present experiments is described in detail in the earlier work of Smith & Glezer (1998) and is shown in figure 1. The jet is synthesized by the time-periodic formation of successive vortex pairs that are formed at the edges of the rectangular orifice. The orifice plate forms one of the walls of an otherwise sealed cavity, and the hydrodynamic impulse that is necessary to form each vortex is provided by the motion of a diaphragm that is mounted on one of the cavity walls. As noted by Smith & Glezer (1998), and similar to the formation of axisymmetric vortex rings (e.g. Didden 1979; Glezer 1988), the formation of each vortex pair may be characterized by the dimensionless stroke length L_0/h ($L_0 = \int_0^\tau u_0(t)\mathrm{d}t$ where $u_0(t)$ is the cross-stream average orifice velocity of the synthetic jet, and $\tau = \frac{1}{2}T$ is the time of discharge or half the period of the diaphragm motion). Note that L_0/h is the inverse of the Strouhal number $S_t = fh/U_0$ and the stroke length is used to emphasize the role of the vortex pairs in the evolution of the jet. An additional parameter is the synthetic jet Reynolds number $Re_{U_0} = U_0h/\nu$ based on the actuator orifice height h and the time-averaged downstream orifice velocity $U_0 = L_0/T$.

An isolated jet actuator is calibrated by simultaneous measurements of the jet velocity and the corresponding amplitude of the oscillating cavity pressure. The jet velocity is measured on the centreline of the orifice using a miniature hot-wire sensor whereas the instantaneous cavity pressure is measured using a commercial high-frequency (55 kHz) piezo-resistive pressure sensor that is built into one of the cavity walls. For a given operating frequency (a separate calibration is performed at each operating frequency), Re_{U_0} is calculated using the centreline velocity data (assuming uniform orifice flow) and is found to increase approximately linearly with the cavity pressure amplitude (Smith 1999). However, for a given cavity pressure, this calibration procedure does not account for cross-stream variations in the synthetic jet orifice speed that are affected by the co-flowing primary jet or the addition of an orifice step. These effects were assessed over a range of operating conditions by means of high-resolution PIV measurements in a domain that contains the jet orifice. The flow through the edges of the measurement domain is integrated to yield a measure of the average orifice velocity. Figure 4 shows that for a given actuation frequency and a setting of the jet cavity pressure for which the calibration Reynolds number is 350, the synthetic jet Reynolds number increases with step size by up to 25% at a fixed co-flowing jet speed. This is ostensibly a result of a larger pressure gradient across the orifice and a non-uniform orifice velocity distribution. For a given step size, an increase in the speed of the primary jet leads to a nominal decrease of 10% in Re_{U_0} over the range of primary jet velocities reported here. Therefore, all the values of Re_{U_0} that are quoted in this paper are derived from PIV measurements and reflect the actual experimental conditions.

2.3. *Velocity measurements*

The bulk of the velocity measurements in the present work are obtained using PIV. The optical set-up consists of a pair of 50 mJ NdYAg lasers that can be triggered in time intervals as short as 1 μs, an adjustable lens system that can produce a sheet of light of variable thickness and width, and a CCD camera having a square 10^6-element sensor. Distributions of the two orthogonal velocity components in planar cross-sections of the flow field are obtained from successive image pairs of seed particles (smoke or theatre fog particles of 5–20 μm in diameter introduced at the
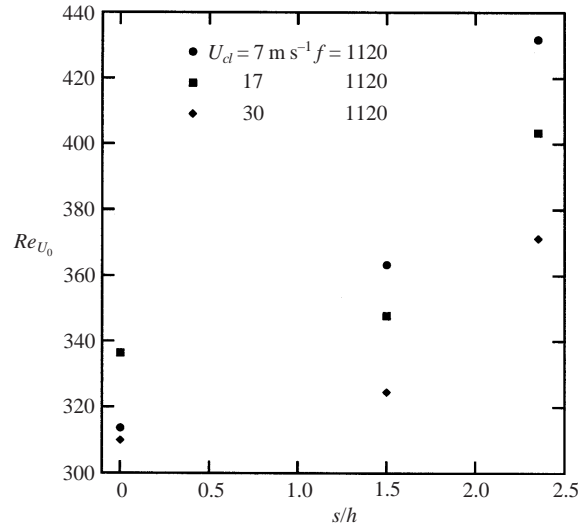
FIGURE 4. Variation of the synthetic jet Reynolds number with step size
and primary jet centreline velocity.

blower inlet) using cross-correlation algorithms (Adrian 1991). The pulsed lasers and the camera are controlled by a dedicated laboratory computer using synchronizing electronic hardware and accompanying software (TSI Inc.) that allow for variation of the delay time between successive image pairs. In the present experiments, the laser and the camera are phase-locked to the driving signal of the actuator and a phase-averaged measurement is typically computed from 50 image pairs.

Three different magnifications result in a field of view measuring $0.46H$, $1.56H$ or $2.75H$ on the side (H is the height of the primary jet conduit), corresponding to 6.3, 21 and 37 μm pixel^{-1}. For each magnification, the resulting square image grid consists of 64×64 data points. The interrogation domain that is used for the computation of the cross-correlation measures 32 pixels on the side. The time delay between successive images is selected such that the maximum mean velocity results in displacements that are nominally a quarter of the length of the interrogation domain (8 pixels). Assuming subpixel resolution (Raffel, Willert & Kompenhans 1998), the resulting velocity resolution is about 1.25% of the maximum average velocity. As noted above, the flow is seeded using theatre fog injected at the inlet to the blower of the primary jet (which results in uniform seeding inside the conduit at the exit plane). The ambient fluid that is entrained into the primary jet on both sides is independently seeded by injecting fog ahead of the experimental run to allow velocity fluctuations associated with the seeding to subside. Distributions of the spanwise vorticity component are computed from the two-dimensional velocity field. The limited spatial resolution of the velocity data may result in the attenuation of the vorticity magnitude and therefore, in the present work, the vorticity distributions are primarily used for qualitative assessment of the interaction between the primary and control jets.

In addition to the PIV field measurements, two-component hot-wire anemometry is used for velocity measurements requiring high temporal resolution or large spatial domains. The two-sensor ($\times$-wire) probe that is used to measure velocity distributions in the vectored primary jet is pitched such that its axis is co-linear with the mean flow so that the instantaneous variations in the velocity vector are within the calibration range of the sensor.

3. The near-field structure of the synthetic jet

This section describes some of the near-field features of synthetic jets that are relevant to its interaction with other flows. The flow in the near field of a synthetic jet issuing into quiescent surroundings is dominated by the temporally alternating blowing and suction strokes that occur during each actuation cycle (Smith & Glezer 1998). Whereas the nominally two-dimensional flow during the suction stroke is similar to the flow induced by a sink that is coincident with the jet orifice, the flow during the blowing stroke is jet-like and is primarily confined to a finite sector that is symmetric about the jet centreline. The time-periodic reversal in flow direction along the jet centreline during the blowing and suction strokes leads to the formation of a stagnation (saddle) point on the centreline downstream of the orifice. It is noted that the spatial position of stagnation points in a phase-averaged velocity field can vary with time. The presence of this stagnation point is evident in maps of flow streamlines that are computed from the phase-averaged PIV velocity and are shown in figure 5. The streamwise extent of the measurement domain is $0 < x/h < 37.3$ and it is centred about the jet centreline. The streamline maps in figure 5 are computed at the peak of the suction stroke $t/T = 0.75$ (T is the actuation period and $t = 0$ is the beginning of the blowing stroke). The jet Reynolds number is $Re_{U_0} = 300$, and the driving frequency is $f = 600\,\text{Hz}$ ($L_0/h = 29.1$). The stream function increment between adjacent streamlines is $0.25Q_0$ ($Q_0 = hU_0$). The earlier work of Smith & Glezer (1998) and Smith, Trautman & Glezer (1999) has shown that while the near-field evolution of synthetic jets (e.g. the vortex pair trajectory) depends primarily on L_0/h, downstream of the vortex pair breakdown, the synthetic jet flow is strongly dependent on the jet Reynolds number. In the data shown in figure 5(*a*), a stagnation point is present at $x/h = 5$ (Smith 1999 demonstrated that the streamwise location of the stagnation point increases with L_0/h). Corresponding vorticity distributions (not shown) indicate that the stagnation point forms between the vortex pair and the exit plane. The stagnation streamlines that are nearly parallel to the exit plane separate between the flow away from the exit plane and flow toward the jet orifice. It is clear that the suction flow is restricted to the narrow domain that is bounded by the top and bottom branches of the stagnation streamline and the exit plane of the jet and that the stream tube through which this fluid flows is narrower when L_0/h is smaller.

Because the orifice of the synthetic jet that is used in the present vectoring experiments is not symmetric about its cross-stream centreline owing to the presence of the cavity wall (figure 2*b*), the baseline flow is somewhat asymmetric near the orifice and the jet is slightly tilted upward in the far field of figure 5(*a*). However, calculations of the volume flow rate between each of the upper and lower branches of the stagnation streamline and the wall show that the suction flow into the jet orifice is the same on both sides of the jet centreline. Furthermore, the amount of fluid that is entrained into the jet column in the far field (i.e. downstream of the upper and lower branches of the stagnation streamline) is also symmetric with respect to the jet centreline. Farther downstream, the fluid on both sides of the centreline is nominally directed towards the jet orifice and then turns around in the streamwise direction near the cross-stream edges of the jet.

The symmetry of the flow that is transported towards the orifice during the suction stroke can be effectively manipulated on either side of the jet centreline by extending one of the edges of the synthetic jet orifice in the downstream direction, as shown
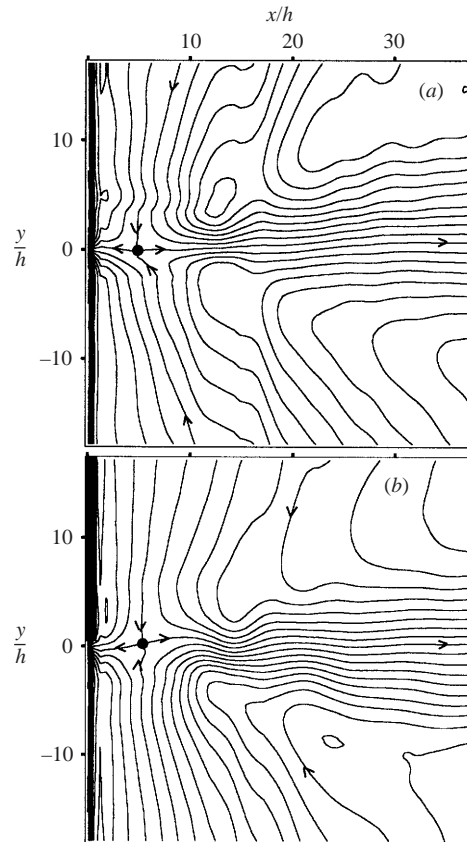
FIGURE 5. Phase-locked streamline maps of a rectangular synthetic jet at $t/T = 0.75$, $Re_{U_0} = 300$, $L_0/h = 29.1$ and $f = 600\,\mathrm{Hz}$, (a) $s/h = 0$, (b) $s/h = 0.6$.

in figure 2(b). The presence of the step restricts the suction flow on that side of the jet centreline and therefore leads to an increase in the flow rate on the opposite side of the jet orifice. The effect of a step that is placed on the top side of the jet orifice and measures $s/h = 0.6$ in the streamwise direction is shown in a phase locked streamline map in figure 5(b). The presence of the step leads to a 50% increase in the suction flow between the exit plane and the stagnation streamline branch below the jet centreline and a corresponding decrease above. In addition, there is a 43% increase in entrainment of far-field fluid into the domain below the jet centreline and downstream of the stagnation streamline compared to the flow without a step. The entrainment into the domain above the jet centreline is unaffected.

These changes in entrainment may be explained by considering the centreline velocity of the synthetic jet with and without a step. Figures 6(a) and 6(b) show pairs of phase-averaged time traces of the streamwise velocity measured at $x/h = 0$ and 1.5, respectively, in the presence and absence of a 1.5h step. These data demonstrate that the phase-averaged streamwise velocity at both streamwise stations remains virtually invariant when the step is added. Now, consider that in the presence of a step above the orifice, during the suction stroke, the fluid approaching from the top (step) side encounters the velocity field associated with the trace shown in figure 6(b), while the fluid below encounters the velocity field depicted in figure 6(a). The large mismatch in both the magnitude and duration of the suction flow at these two locations results
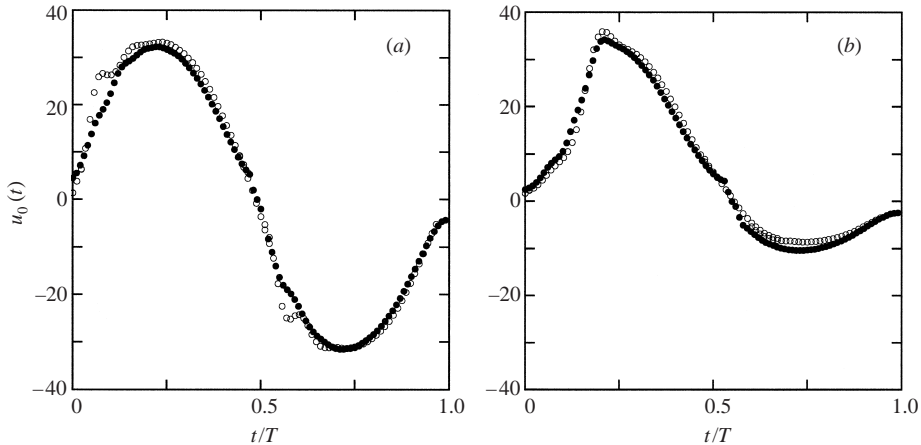
FIGURE 6. Phase locked velocity traces on the centreline of the synthetic jet at (*a*) $x/h = 0$ and (*b*) $x/h = 1.5$. ○, synthetic jet without a step; ●, synthetic jet with $s/h = 1.5$ step.

in the asymmetry of the entrained flow about the jet centreline in figure 5(*b*). This ability to control the symmetry of the suction flow is very useful in jet vectoring, as shown in §§4 and 5 below.

4. The time-averaged flow field of the vectored jet

Schlieren images of the unforced and forced primary jet described in §2.1 are shown in figures 7(*a*) and 7(*b*). The centreline velocity of the unforced jet is $7\,\mathrm{m\,s^{-1}}$, and the synthetic jet is operating at $Re_{U_0} = 380$, $L_0/h = 19.7$ ($f = 1120\,\mathrm{Hz}$), with a step $s/h = 1.5$. It is evident that the flow within the conduit is laminar, and the Kelvin–Helmholtz (K-H) instability of the primary jet shear layers leads to the formation of vortical structures that are symmetric about the jet centreline for the unforced jet. The image of the forced flow shows that the primary jet is vectored toward the synthetic jet at a mean angle of approximately 30°.

The proximity of the synthetic jet to the primary jet allows the two jets to interact such that during the suction stroke, the synthetic jet draws some of its fluid from the primary jet. This interaction results in the formation of a low-pressure region between the two jets and the acceleration of the primary jet fluid near the upper conduit wall (figure 8). As shown below, the pressure field induced by the interaction between the jets leads to the turning of the flow inside the conduit upstream of the exit plane. The cross-stream momentum of the vectored primary jet balances a normal force on the conduit.

The time-averaged interaction between the jets downstream of the exit plane is measured using two-component hot-wire anemometry. Cross-stream distributions of the mean streamwise velocity component of the forced and unforced flows are measured at 11 streamwise stations between $0.79 < x/H < 11.8$ and are plotted in similarity coordinates in figures 9(*a*) and 9(*b*). Since the characteristic cross-stream width of turbulent, two-dimensional jets increases linearly with downstream distance, the cross-stream (*y*) coordinate is normalized by the streamwise distance from the jet exit plane (*x*). Similar to measurements reported by other investigators (e.g. Gutmark & Wygnanski 1976), the unforced jet (figure 9*a*) becomes self-similar for $x/H > 6$. In the forced jet (figure 9*b*) the maximae of the streamwise velocity distributions occur at the same dimensionless cross-stream coordinate for $2.46 < x/H < 11.8$, indicating
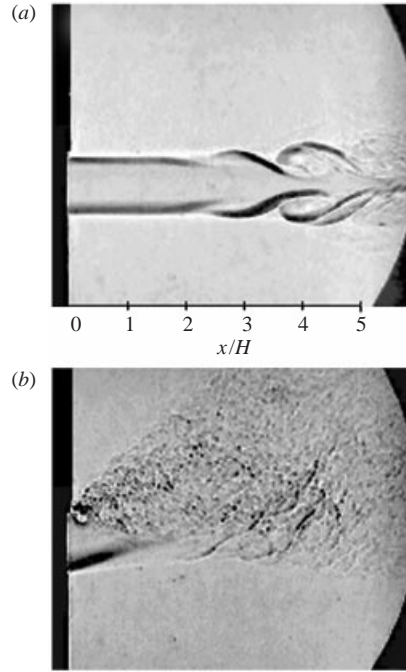
(*a*)

x/H

(*b*)

FIGURE 7. Schlieren images of synthetic jet vectoring: (*a*) unforced primary jet $U_{cl} = 7\,\text{m\,s}^{-1}$; (*b*) forced at $Re_{U_0} = 380$, $L_0/h = 19.7$, $f = 1120\,\text{Hz}$, $s/h = 1.5$.
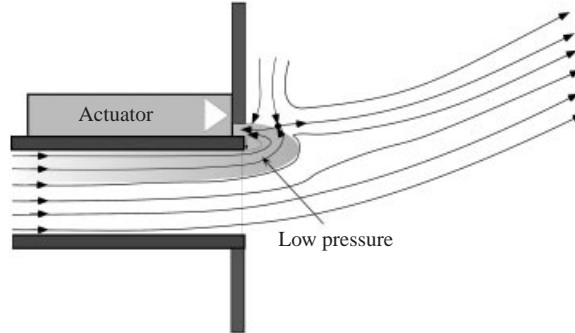

FIGURE 8. Schematic description of flow vectoring induced by the synthetic jet.

that the vectoring angle does not change appreciably within this domain. However, the cross-stream spreading of the shear layers on each side of the forced jet is not symmetric. This can be seen more clearly by considering the width of the vectored jet, which is commonly taken to be the cross-stream location at which the streamwise velocity is equal to half the maximum value. In figure 10, the cross-stream locations (one on either side of the jet) of the half-velocity points are plotted with respect to their downstream positions. It is remarkable that the forced side of the jet spreads linearly with x, while the spreading rate of the unforced side is smaller (a fractional power of x) up to $x/H = 8$. It appears that for $x/H > 8$, the unforced shear layer begins to spread linearly with x. In addition, as a result of the forcing, the primary jet at $x/H = 10$ is twice as wide as the unforced jet. Spanwise variations in the velocity field of the primary jet downstream of the exit plane ($0.8 < x/H < 6.3$) in the presence of actuation are discussed in some detail in an earlier paper (Smith
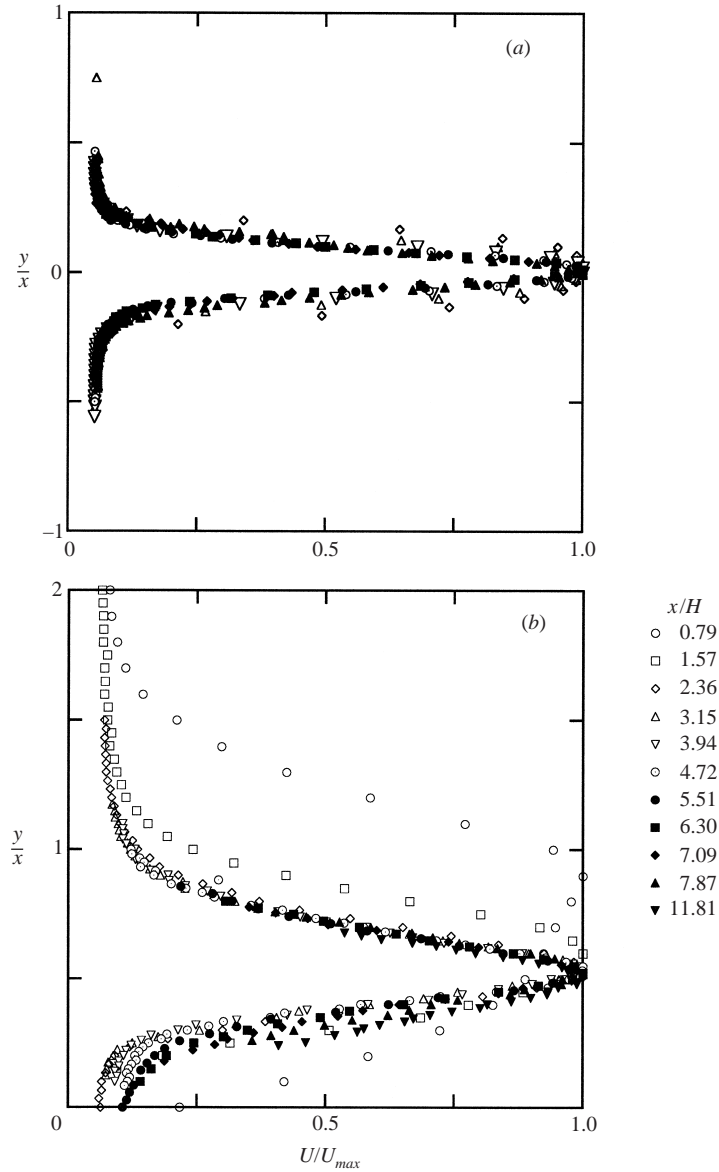
FIGURE 9. Cross-stream distributions of streamwise velocity component of the primary jet:
(*a*) unforced; (*b*) forced ($Re_{U_0} = 380$, $L_0/h = 19.7$, $f = 1120\,\mathrm{Hz}$ and $s/h = 1.5$).

& Glezer 1997). Although the aspect ratio of the baseline primary jet decreases to approximately 1 at $x/H = 6.3$, it is almost invariant within the domain of the present measurements. Owing to the finite spanwise extent of both the primary and synthetic jets, the vectoring of the primary jet is not spanwise uniform and at $x/H = 3.5$, the vectoring angle near its spanwise edges is approximately 50% lower than at the centreline. In the present work, the nominally two-dimensional interaction between the primary and synthetic jets and the flow mechanisms that result in the vectoring of the primary flow are investigated near the exit plane of the primary jet (i.e. $x/H < 2$) where spanwise variations of the vectored flow (not including edge effects) are reasonably small.
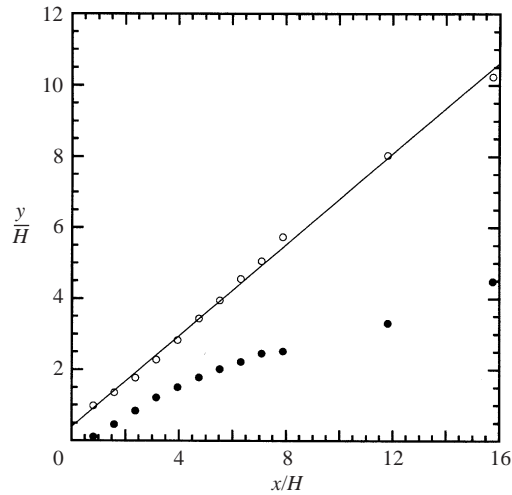
Figure 10. Locations of the upper (◯) and lower (●) jet boundaries based on
half the maximum velocity.

The substantial increases in small-scale motions within the forced primary jet
suggest that mixing in the jet shear layer is enhanced. Direct excitation of dissipative
scales within a square jet using cartilevered piezoelectric actuators was reported by
Wiltse & Glezer (1998). They show that as a result of the excitation, the dissipation
within the forced segment of the jet shear layer increases by one to two orders of
magnitude over a broad streamwise domain. A similar effect takes place as a result
of synthetic jet forcing, as confirmed by power spectra measured at $x/H = 3.15$
within the shear layer of the unforced jet, and in the upper (forced) and lower
(unforced) shear layers of the vectored jet at cross-stream positions corresponding to
$U(y)/U_{cl} = 0.73$ (figure 11). Note that for clarity, the spectra (*b*) and (*c*) are displaced
downward by two and four decades, respectively. The operating frequency of the
actuator (970 Hz) is nearly an order of magnitude higher than the natural unstable
frequency band of the jet shear layer (centred around 135 Hz in the unforced jet).

The most unstable (K-H) frequency of the unforced jet and its higher harmonics
are prominent in the spectrum of the unforced jet (figure 11*c*). By contrast, the
K-H instability is completely suppressed by the forcing, as indicated by the spectrum
of the forced shear layer of the vectored jet (figure 11*a*). Small-scale motions are
enhanced over a broad range of frequencies and it appears that an inertial subrange
is established for 100 Hz $< f <$ 1000 Hz where the spectral peak at the actuator
frequency is at the low-frequency end of this range. While spectral components of the
unstable K-H frequency of the unvectored flow and its first harmonic are also present
in the spectrum of the lower (unforced) shear layer of the vectored jet, the frequency
of these peaks is somewhat lower than in the unvectored flow. This is consistent with
broadening of the shear layers in the forced jet, as is evident in the schlieren image
in figure 7(*b*). The substantial broadband increase in the magnitude of small-scale
motions and the presence of a spectral peak at the forcing frequency suggest that
the forcing effect is transmitted through the core of the primary jet, presumably by
pressure fluctuations (similar effects in the wake of a circular cylinder were reported
by Amitay, Smith & Glezer (1998).

The PIV data within the largest field of view $0.22 < x/H < 2.53$ and $-0.81 <
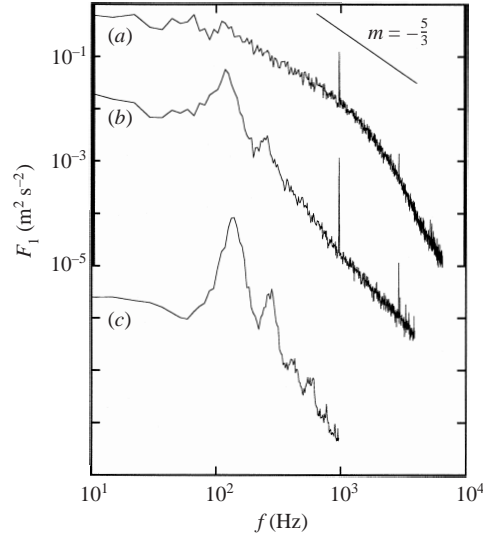y/H < 1.94$ are used to determine the far-field features of the vectored jet. Streamline

FIGURE 11. Power spectra of the streamwise velocity component measured at the cross-stream locations corresponding to $U/U_{cl} = 0.73$: (a) forced side of vectored jet ($f = 970$ Hz); (b) unforced side of vectored jet; (c) in the unforced jet.
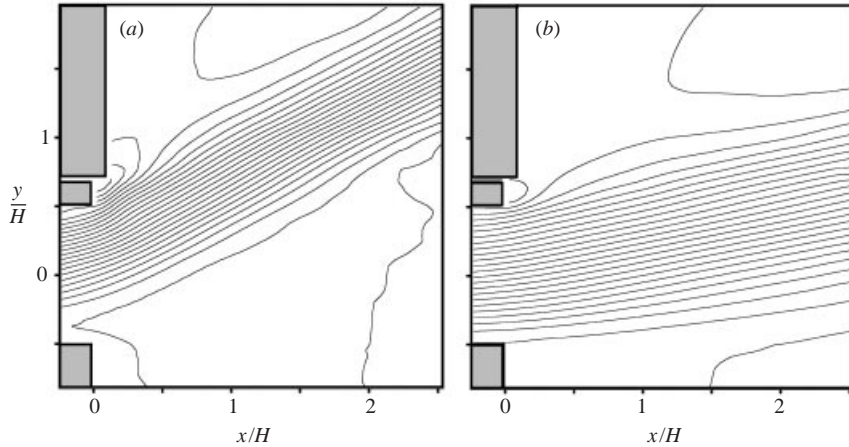

FIGURE 12. Streamline maps of the forced flow for (a) $U_{cl} = 7\,\text{m s}^{-1}$ and (b) $17\,\text{m s}^{-1}$. Contour increments are 5% of the volume flow rate of the unforced flow ($Re_{U_0} = 380$, $L_0/h = 19.7$, $f = 1120$ Hz and $s/h = 1.5$).

maps of the mean flow of the forced ($Re_{U_0} = 380$, $L_0/h = 19.7$, $s/h = 1.5$) primary jet for the range of centreline velocities $5 \leqslant U_{cl} \leqslant 27\,\text{m s}^{-1}$ are computed. Figures 12(a) and 12(b) show the streamline maps for $U_{cl} = 7$ and $17\,\text{m s}^{-1}$, respectively. The stream function is determined by integrating the velocity field from the bottom right-hand corner of the measurement domain. This prevents the need to integrate across the flow boundaries, where the velocity field cannot be measured because of reflections of the laser light off the surface. At this magnification, the details of the wall boundary layers or of the synthetic jet flow cannot be resolved. With the synthetic jet input nominally unchanged (within the calibration errors discussed in §2.2), larger primary jet velocities result in smaller vectoring angles (30° for $U_{cl} = 7\,\text{m s}^{-1}$ and 12° for
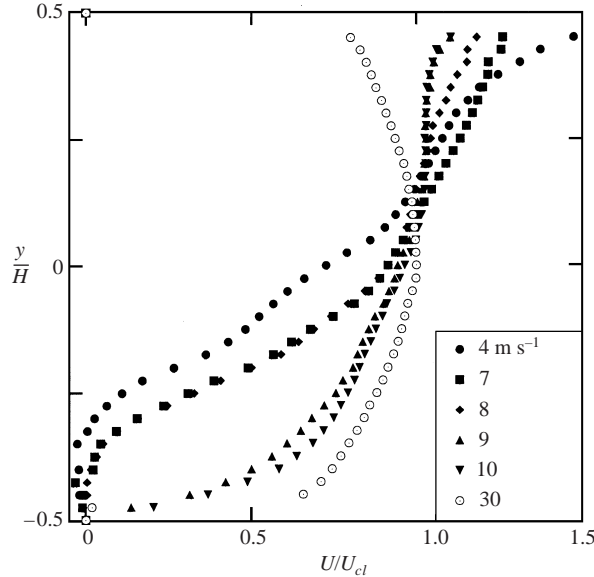
FIGURE 13. Cross-stream distributions of U for $Re_{U_0} = 363$, $L_0/h = 18.8$,
$f = 1120\,\mathrm{Hz}$ and $s/h = 1.5$.

$U_{cl} = 17\,\mathrm{m\,s^{-1}}$) and a larger cross-stream force, as shown below. The present data show that the primary jet begins to turn upstream of the exit plane, and the change in the flow direction is nearly completed at the exit plane. As shown in figure 13, when the flow in the jet conduit is laminar (i.e. $U_{cl} < 8\,\mathrm{m\,s^{-1}}$), the forced jet becomes separated from the lower conduit wall upstream of the exit plane.

Some of the details of the mean flow inside the conduit and the near field are investigated using phase-averaged PIV measurements in the domain $-0.83 \leqslant x/H \leqslant 0.75$ and $-0.6 \leqslant y/H \leqslant 0.98$. A magnification of $21\,\mu\mathrm{m\,pixel^{-1}}$ is used to resolve the flow features inside the conduit and to extend the measurement domain sufficiently upstream and downstream to capture the beginning and end of the vectoring. The velocity data along with surface pressure distributions are used to calculate resultant forces using a control volume which is bounded by the conduit walls, the exit plane, and the upstream end of the measurement domain ($x/H = -0.83$). When the vertical force is computed, the downstream end of the control volume is extended to include the step. It is noted that the unsteady terms of the control volume equation are estimated using the phase-averaged data and are insignificant compared to the time-averaged terms. The present data are averaged over 100–150 realizations, and when the conduit flow is turbulent the standard deviation of the mean velocity is about 10%.

Cross-stream distributions of the time-averaged streamwise (U) velocity component at the exit plane of the primary jet are shown in figure 13 for several centreline velocities of the unforced primary jet. In each of these cases, $Re_{U_0} = 363$, $L_0/h = 18.8$ ($f = 1120\,\mathrm{Hz}$) and $s/h = 1.5$. It is clear from figure 13 that at the lower speeds, the flow is separated at the lower wall of the conduit, although no appreciable reverse flow is measured. As noted above, following turbulent transition ($U_{cl} \approx 8\,\mathrm{m\,s^{-1}}$), the flow does not separate, and the velocity near the lower wall resembles the unforced conduit flow. When $U_{cl} = 30\,\mathrm{m\,s^{-1}}$, the effect of the forcing on the streamwise component of velocity is virtually undetectable, and the profile appears to be symmetric about $y = 0$. The cross-stream velocity component (not shown, see
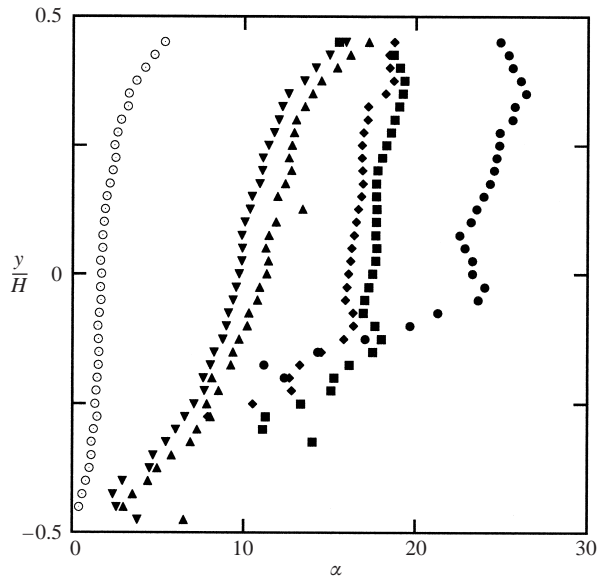
FIGURE 14. Cross-stream variation of the flow angle at the exit plane of the forced jet. $Re_{U_0} = 363$, $L_0/h = 18.8$, $f = 1120\,\text{Hz}$ with $s/h = 1.5$. Symbols as in figure 13.

Smith 1999) increases almost linearly toward the upper side of the conduit (past the separated region in the laminar cases) where $\partial V/\partial y$ decreases with increasing primary jet speed. Even at the highest speed, the forcing results in a non-zero cross-stream flow near the upper conduit wall.

Cross-stream variation of the angle of the vectored flow across the jet exit is computed for $|V| > 0.5\,\text{m s}^{-1}$, and is shown in figure 14. The flow angle is nearly uniform or slowly increasing toward the upper conduit wall (the flow angle within the separated region is not included). Note that the vectoring angles at the exit plane are not the same as the final vectoring angles of the mean streamlines in figure 12, indicating that the flow continues to turn in the cross-stream direction downstream of the exit plane. In fact, contours of the local flow angle in figure 15 show that the flow angle nearly doubles within a narrow angular section centred at the upper edge of the jet conduit. These data show that the turning is nearly complete for $x/H > 1$. The strong variation of the flow angle near the synthetic jet orifice is indicative of flow turning around an induced low-pressure region as discussed further below. Ambient fluid is continuously entrained into the shear layers near the edges of the primary jet and this fluid undergoes a rapid change in flow direction.

Since as shown below, the local pressure near the exit plane is reduced owing to the presence of the synthetic jet, it is reasonable to expect that the flow rate through the conduit is altered when forcing is applied. In fact, at low speeds $Re_H < 5500$ (when the conduit flow is laminar) there is a small increase in flow rate. Following transition to turbulence ($U_{cl} \approx 8\,\text{m s}^{-1}$), the reduced exit plane pressure results in a marked increase in the conduit flow rate. The increase becomes larger with step size, and peaks near 9% for $s/h = 2.35$. As the primary jet Reynolds number increases beyond 10^4, the flow rate decreases toward the unforced level. Clearly, the changes in the volume flow rate as a result of the change in load depend on the specific characteristics of the system blower.

The increase in the primary jet flow rate is accompanied by an increase in the flux of streamwise momentum at the exit plane. It is remarkable that even though about half
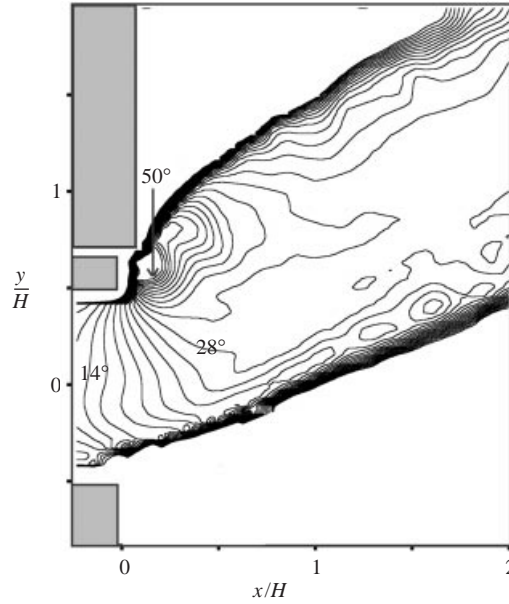
FIGURE 15. Contour map of the flow angle of the vectored jet. Starting contour and contour
increments are 2°. $U_{cl} = 7\,\text{m}\,\text{s}^{-1}$, $Re_{U_0} = 363$, $L_0/h = 18.8$, $f = 1120\,\text{Hz}$ and $s/h = 1.5$.

of the momentum of the vectored jet is in the cross-stream direction, the remaining
streamwise momentum is larger than in the unforced flow (not shown). While the flow
rate in the laminar conduit flow is substantially unchanged, the increase in streamwise
momentum is as high as 20% of the unforced value and is attributed to changes in
the velocity profile.

As noted above, the resultant force exerted on the conduit wall by the vectored
jet is computed using a control volume that is bounded by the conduit walls, the
exit plane, and the upstream end of the measurement domain ($x/H = -0.83$). The
streamwise variation of this force is computed by varying the downstream end of the
control volume through the exit plane of the primary jet. In addition to the velocity
measurements, the distributions of static pressure along the upper and lower conduit
surfaces are measured independently using pressure taps (cf. §2). Figure 16 shows the
streamwise distributions of the resultant vertical force on the segments of the top and
bottom surface that are bounded by the upstream extent of the data ($x/H = -3$) and
by the downstream edge of a control volume having a variable streamwise length.
The resulting normal force $F_y(x)$ is computed for the domain $-3 = -x/H = -0.5$ by
streamwise integration of the pressure difference between the upper and lower walls
(closed symbols), and for the domain $-0.82 = x/H = 0.06$ by computing the net flux
of cross-stream momentum

$$J_y(x) = \int_{-H/2}^{H/2} \rho U(x, y) V(x, y)\,\mathrm{d}y$$

using the velocity measurements (open symbols). It is clear that the resultant force
increases with the primary jet velocity (as discussed further in connection with figure 17
below). The pressure data show that the effect of the vectoring is measurable as far
as $2H$ upstream of the exit plane. However, these data also show that most of the
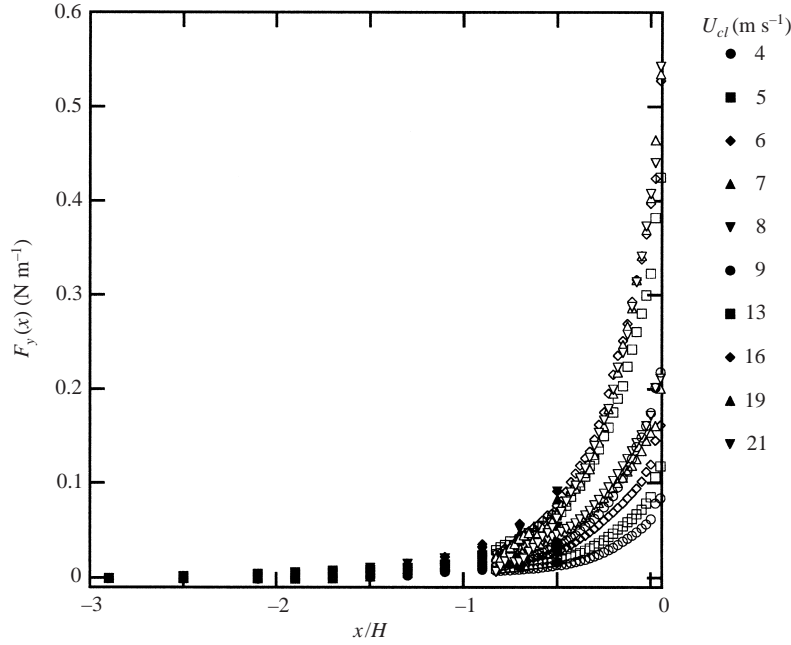contribution to the vectoring force occurs within the domain $-1 < x/H < 0$. The

FIGURE 16. Streamwise variation of vectoring force. Closed and open symbols correspond to pressure and PIV data, respectively. $Re_{U_0} = 363$, $L_0/h = 18.8$, $f = 1120\,\text{Hz}$, $s/h = 1.5$.

discrepancy between the force computed from the surface pressure distribution and from the momentum flux is less than 5% of the maximum value.

As discussed above, the performance of the synthetic jet depends on f, s, and U_0. The dependence of the vectoring force on these variables and on the speed of the primary jet is illustrated in figure 17. These data include three orifice steps ($s/h = 0$, 1.5 and 2.35), four frequencies (700, 720, 900 and 1120 Hz), and synthetic jet Reynolds numbers between 280 and 490. Figure 17 reveals three primary trends: (i) in all cases (fixed s, U_0 and f), the vectoring force initially increases with primary jet speed, and in most cases reaches a maximum that precedes a decrease, (ii) the primary jet speed at which the vectoring force peaks increase with step size and frequency, and (iii) an increase in Re_{U_0} generally results in an increase in the vectoring force. For both high and low Re_{U_0} the maximum force occurs at the same primary jet speed. These findings are consistent with the work of Hammond & Redekopp (1997) who showed that the vectoring force increases with the shear of the primary flow although no maximum was reported (possibly owing to the range of shear studied). More importantly, these authors also reported that the vectoring force increases with the suction flow rate, which for the synthetic jet depends on Re_{U_0}. Therefore, it may be argued that the data of figure 17 indicate that the vectoring force increases with the volume flow rate of primary jet fluid that is diverted by the synthetic jet which in turn depends on the step size and the driving frequency. These effects are discussed in detail in §5 below.

5. The interaction between the synthetic and primary jets

The unsteady interaction between the synthetic jet and the primary jet occurs within a small domain between the jets near the exit plane. In order to resolve the details of the flow structure within this domain, high-magnification PIV images are captured phase-locked to the actuator driving signal at 18 evenly spaced phase increments during the actuator cycle.
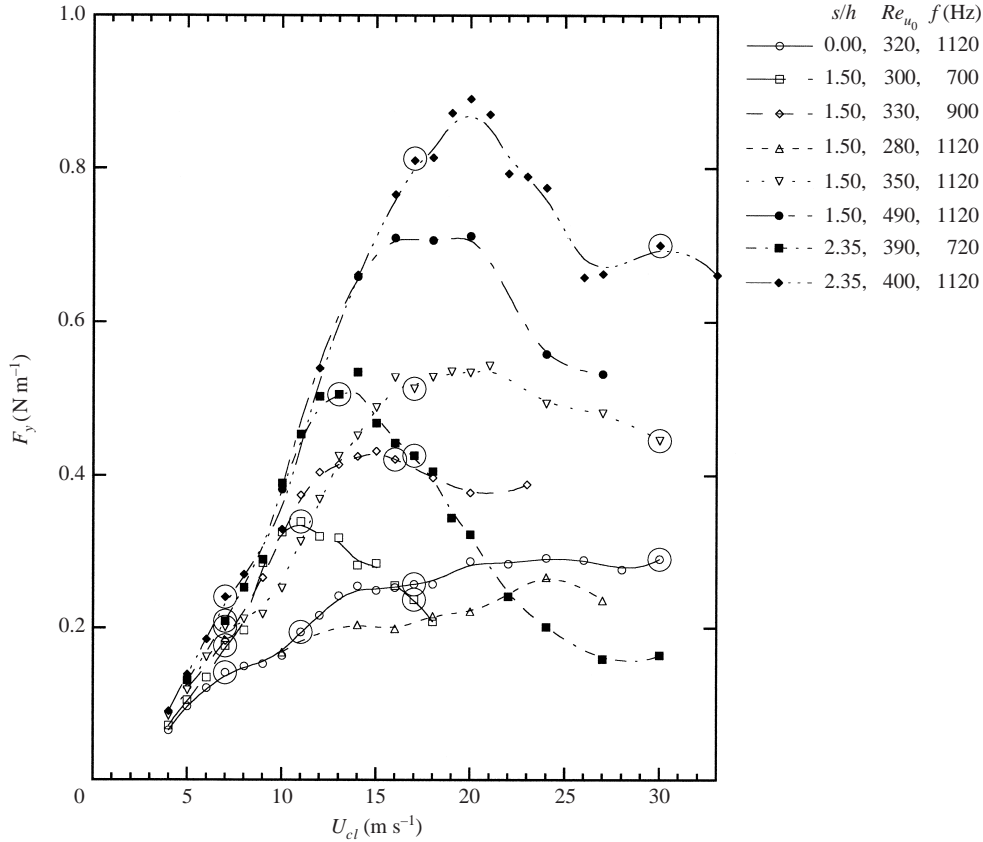
FIGURE 17. Variation of the vectoring force with the primary jet centreline velocity. (Encircled data points indicate that the high-resolution phase-locked measurements were also taken for this case.)

Figure 18 is composed of nine phase-averaged streamline maps measured at equally spaced phase increments ($Re_{U_0} = 314$, $L_0/h = 16.3$, $s/h = 0$ and $U_{cl} = 7\,\mathrm{m\,s^{-1}}$). The start of the blowing stroke of the synthetic jet (Figure 18*a*) is taken to be $t/T = 0$ and the volume flow rate increment between adjacent streamlines is 1% of the flow rate of the unforced primary jet. Note that measurements near the surface (within $0.014H$) are degraded by surface reflections, and therefore are discarded.

As is evident from the streamlines near the bottom right-hand corner of each of the streamline maps, the direction of the primary jet flow outside the interaction region remains relatively unchanged during the full cycle of the synthetic jet. Similar to an isolated synthetic jet (Smith & Glezer 1998) a counter-rotating vortex pair is formed at the beginning of the blowing stroke. The axis of the pair, which is initially in line with the centreline of the synthetic jet (figure 18*c*) tilts toward the primary jet as the vortex pair is convected downstream (figure 18*d*). The streamlines suggest that the lower (CW) vortex is stronger than the upper (CCW) vortex. This may be attributed to a distortion of the velocity profile within the synthetic jet orifice that results in a thinner boundary layer on its bottom edge and thus the roll-up of a vortex core with higher vorticity concentration. The vorticity within the primary jet shear layer is of the opposite sense to the CW vortex, and subsequently leads to the weakening and cancellation of the CW vortex farther downstream. The suction stroke of the actuator begins at $t/T = 0.5$, and results in the formation of a stagnation point downstream
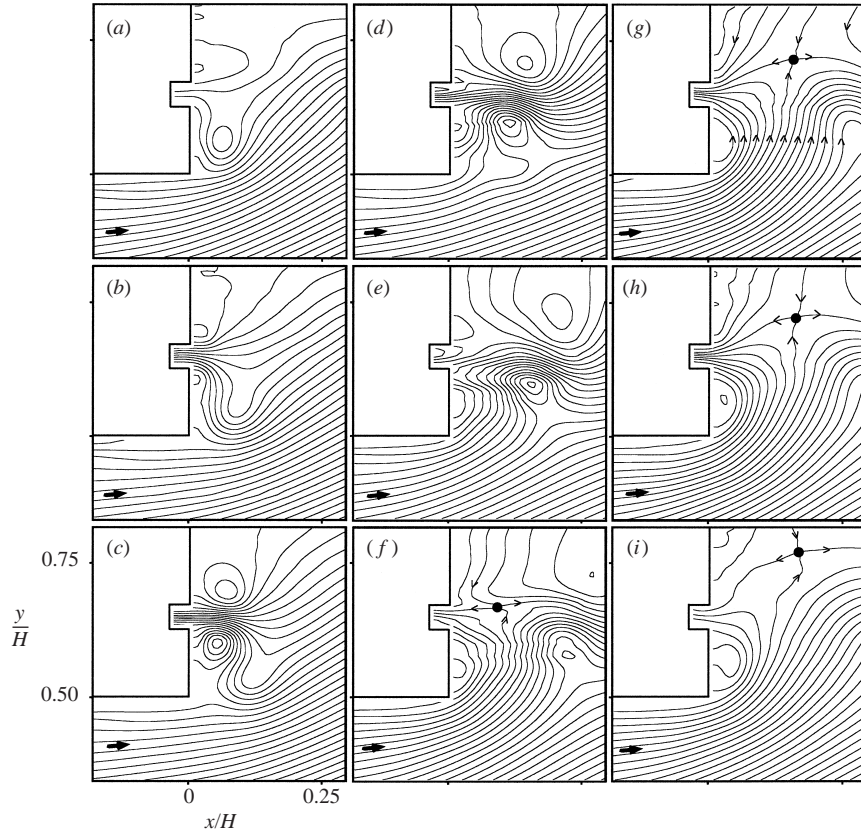
FIGURE 18. Streamline maps of the phase-averaged velocity field in the vicinity of the synthetic jet at nine equal phase increments during the actuator cycle beginning at the start of the blowing stroke ($t/T = 0$). Streamfunction increment corresponds to 1% of the primary jet volume flow rate. Stagnation points are marked in (f) to (i). ($U_{cl} = 7\,\mathrm{m\,s}^{-1}$, $Re_{U_0} = 363$, $L_0/h = 16.3$, $f = 1120\,\mathrm{Hz}$, and $s/h = 0.0$).

of the synthetic jet orifice (figure 18f). The stagnation point that is similar to the stagnation point of an isolated synthetic jet (cf. figure 5) persists during the suction stroke and moves away from the synthetic jet orifice in the cross-stream direction. The stagnation streamlines divide the flow near the synthetic jet into four quadrants: primary jet fluid that is drawn into the actuator; primary jet fluid that continues to move in the downstream direction; ambient fluid that is drawn into the synthetic jet; and ambient fluid that is advected along the primary jet. The streamlines clearly show that during the suction stroke some of the primary jet fluid near the upper surface of the conduit is drawn into the synthetic jet.

Corresponding contour maps of the dimensionless spanwise vorticity ($\omega_z^* = \omega_z h/U_0$) computed from the velocity data are shown in figure 19. Contour levels start at $\omega^* = \pm 0.22$, and the contour increment is $\omega^* = 0.22$ (negative contours are dashed). Except for the conduit boundary layer, vorticity levels within the primary jet are low and do not show up in the contour plots. At the beginning of the blowing stroke (figure 19a), fluid having CCW vorticity from the conduit boundary layer rolls up into a vortex near the edge of the primary jet. This fluid is drawn from the conduit boundary layer during the suction cycle of the synthetic jet and the formation of the vortex leads to induced flow along the exit plane with vorticity of the opposite
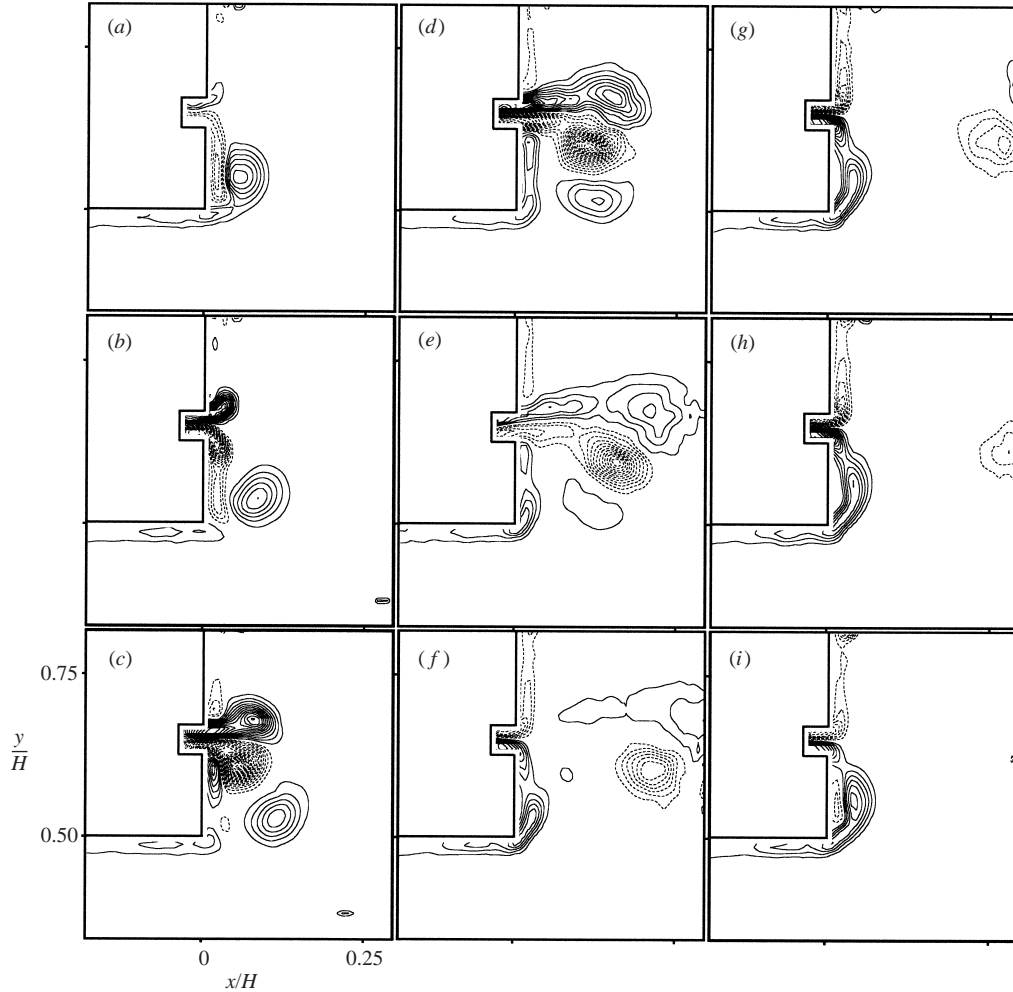
FIGURE 19. Contour maps of the phase-averaged dimensionless spanwise vorticity (ω_z^*) within the interaction domain between the jets. The contour increment is 0.22, and negative contour levels are dashed. Phase increments as in figure 18. ($U_{cl} = 7\,\mathrm{m\,s^{-1}}$, $Re_{U_0} = 363$, $L_0/h = 16.3$, $f = 1120\,\mathrm{Hz}$, and $s/h = 0$).

sense. The blowing cycle of the synthetic jet leads to the release of the CCW vortex that is then advected downstream as a free vortex (figures 19*b* and 19*c*). As for a synthetic jet in a quiescent surrounding, the blowing cycle results in the roll-up of a counter-rotating vortex pair that is accompanied by the formation of vorticity of the opposite sense within the wall boundary layers on either side of the synthetic jet orifice (figures 19*c* and 19*d*). As noted above, at $t/T = 0.33$ (figure 19*d*), the CW vortex of the pair is stronger, and, as a result, the axis of the pair tilts toward the primary jet as the vortex pair is advected downstream. Between $t/T = 0.33$ and $t/T = 0.56$ (figures 19*d* and 19*f*), the CCW vortex weakens rapidly and its vorticity diffuses away from the core.

At the beginning of the suction stroke ($t/T = 0.56$, figure 19*f*), the synthetic jet CW vortex is approximately $0.25H$ downstream from the exit plane and the suction motion along the exit plane is accompanied by the formation of boundary layers having vorticity concentrations of opposite sense on either side of the orifice that
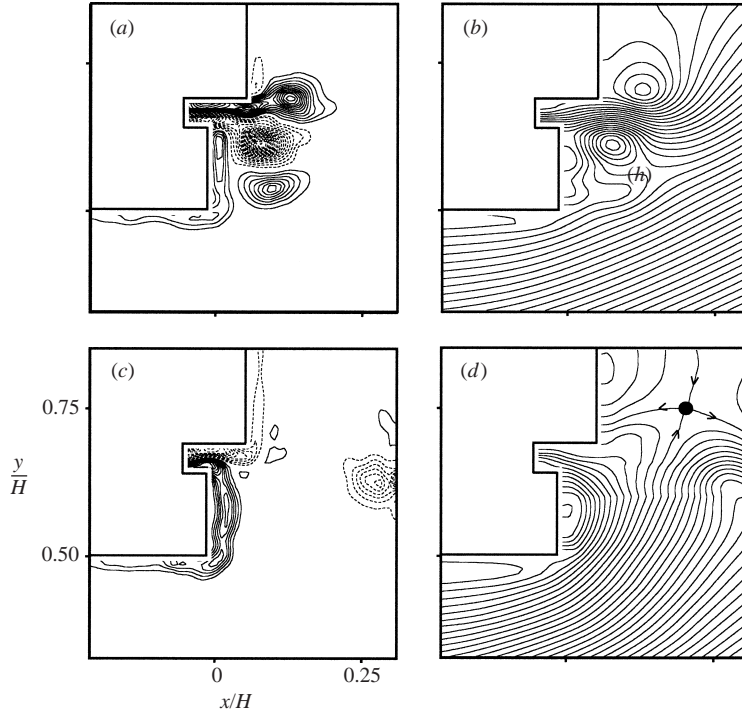
FIGURE 20. (*a*), (*c*) Vorticity and (*b*), (*d*) streamline maps ($U_{cl} = 7\,\mathrm{m\,s}^{-1}$, $Re_{U_0} = 363$, $L_0/h = 18.8$, $f = 1120\,\mathrm{Hz}$, and $s/h = 1.5$) during the blowing stroke ($t/T = 0.33$, (*a*) and (*b*)) and suction stroke ($t/T = 0.67$, (*c*) and (*d*)). Contour increments as in figures 18 and 19, respectively.

intensify as the suction stroke reaches its peak (figure 19*h*). It appears that the induced suction velocity near the surface between the primary jet and the synthetic jet is stronger than above the synthetic jet as is evidenced by the magnitude of vorticity concentration there.

Figure 17 clearly shows that the addition of a step to the synthetic jet orifice results in a larger vectoring force. The effect of a stepped orifice ($s/h = 1.5$) on the interaction between the jets is shown in figure 20 using phase-averaged streamlines (on the right-hand side) and vorticity contour maps (on the left-hand side) during the blowing and suction strokes ($t/T = 0.33$ and 0.67, respectively). Compared to figure 19(*d*) the vortex pair in figure 20(*a*) is tilted more toward the primary jet and the CCW vortex is somewhat less diffused. The streamline maps indicate a stronger vectoring effect than in the absence of the step. In particular, during the suction stroke significantly less fluid is drawn into the synthetic jet from the domain above the step, and in fact the bulk of the synthetic jet fluid is drawn from the primary jet. As discussed above, the stepped orifice leads to an increase in the volume flow rate and the flux of streamwise momentum of the primary jet as well as to an increase in the vectoring force.

The effect of the step size on the amount of fluid that is drawn from the primary jet is shown in figure 21. The total volume flow rate into the synthetic jet, $Q_{sj}(t)$, is determined from the balance of the flow rate through the measurement domain. The volume flow rate of primary jet fluid that is entrained by the synthetic jet is computed using the phase-averaged stream function. The difference between the magnitude of the stream function at the stagnation point and at the upper surface of the primary
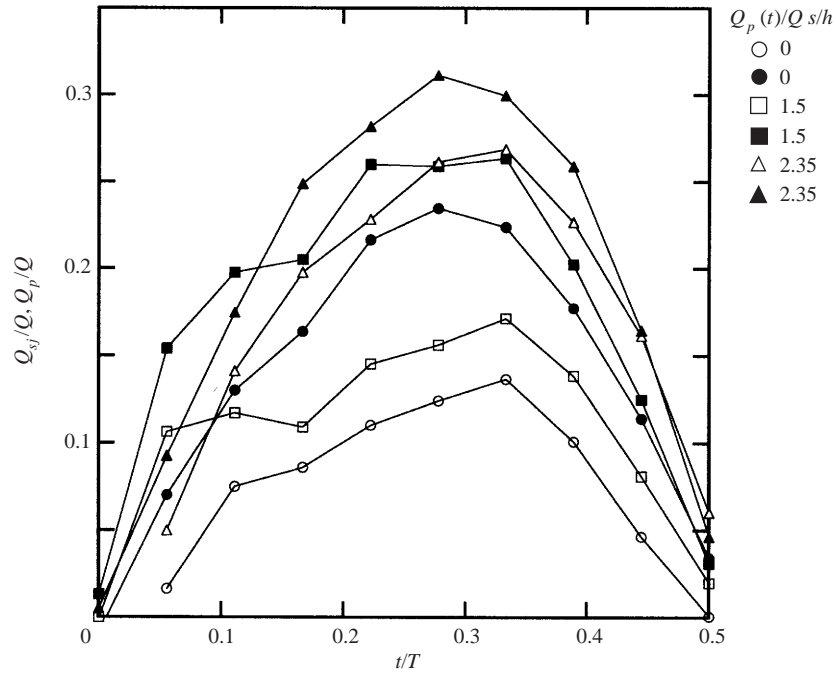
FIGURE 21. The variation with phase during the suction stroke of normalized Q_{sj} (the total flow rate into the synthetic jet actuator, closed symbols) and Q_p (entrained primary jet fluid, open symbols) for $U_{cl} = 7 \, \text{m s}^{-1}$, $f = 1120 \, \text{Hz}$. Q is the volume flow rate of the primary jet.
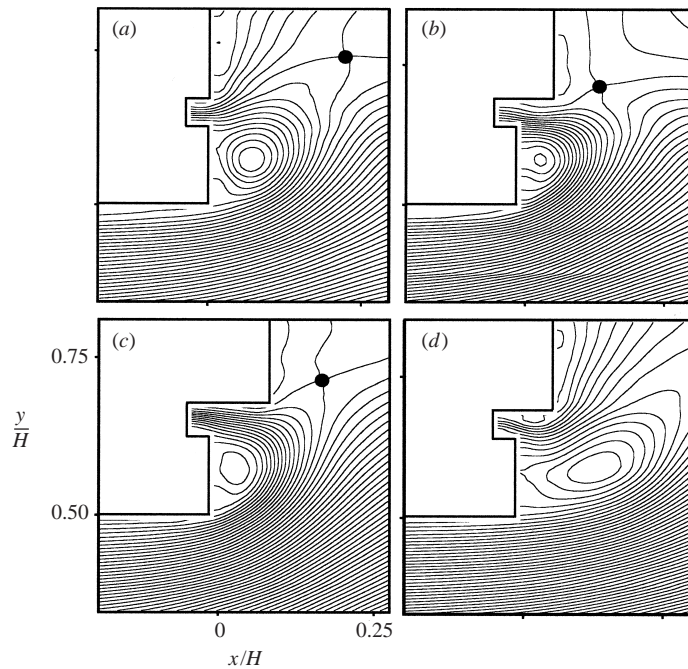

FIGURE 22. Streamlines maps at $t/T = 0.79$ for $U_{cl} = 17 \, \text{m s}^{-1}$, $f = 1120 \, \text{Hz}$, (*a*) $s/h = 0$, (*b*) $s/h = 1.5$, (*c*) $s/h = 2.35$, and (*d*) 700 Hz, $s/h = 1.5$. Streamline increment corresponds to 0.5% of primary jet volume flow rate.

jet conduit is defined as $Q_p(t)$ and is plotted (open symbols) along with $Q_{sj}(t)$ (closed symbols) for different step sizes. As discussed in §2, the Reynolds number of the synthetic jet increases with step size, and hence Q_{sj} also increases. At the same time, the volume fraction of the synthetic jet fluid that originates in the primary jet (Q_p/Q_{sj}) also increases with step size such that for $s/h = 2.35$ the peak volume fraction is over 80%.

At higher primary jet speed (e.g. $U_{cl} = 17\,\mathrm{m\,s^{-1}}$), the flow rate through the stream tube bounded by the upper conduit wall and the stagnation streamline increases, and the separated flow around the edge of the conduit forms a recirculation region (and a CCW vortex). This is illustrated in the streamline map in figure 22(a) ($s/h = 0.0$) which shows that only part of the fluid that enters the region bounded by the stagnation streamline and the wall is actually drawn into the synthetic jet orifice. This is reflected in the magnitude of the cycle-averaged entrained flow $\bar{Q}_p$ (Smith 1999) which is $0.33\bar{Q}_{sj}$ compared to $0.54\bar{Q}_{sj}$ for $U_{cl} = 7\,\mathrm{m\,s^{-1}}$. At the end of the suction stroke, the CCW vortex is advected downstream similar to the vortex in figure 19(b). The addition of a step at the same primary jet speed ($s/h = 1.5$, figure 22b) results in an increase in the fraction of the synthetic jet fluid that is drawn from the primary jet ($\bar{Q}_p/\bar{Q}_{sj} = 0.67$) and in a reduction in the size of the recirculating flow between the edges of the primary and synthetic jets. As noted above, the vectoring angle of the primary jet increases and as a result, the stagnation point moves closer to the synthetic jet. However, an additional increase in the step size to $2.35h$ (figure 22c) does not have a significant effect on the streamline map compared to figure 22(b), and results in a modest increase in $\bar{Q}_p/\bar{Q}_{sj}$ to 0.78. Nevertheless, as shown in figure 17, the larger step results in a considerably larger resultant force, which may be attributed to larger Re_{U_0}, and may also be due to the extended surface on which the pressure acts.

As shown by Smith & Glezer (1998), the streamwise velocity is almost time harmonic with zero-mean at the exit plane of the synthetic jet. The streamwise domain over which these flow oscillations decay scales with L_0. In figure 22(d), L_0 is increased by 40% (by lowering the synthetic jet frequency to 700 Hz) while keeping s/h unchanged ($s/h = 1.5$). As is evident from the streamline map, the stagnation point that is formed during the suction stroke is farther downstream (and in fact out of the present measurement domain) and the recirculation region extends in the streamwise direction through $x/H = 0.25$, leading to a significant reduction in the volume fraction of the primary jet fluid that is drawn into the synthetic jet ($\bar{Q}_p/\bar{Q}_{sj} = 0.077$). At the same time, a larger fraction of the synthetic jet fluid is drawn from the domain above the synthetic jet orifice. The reduction in the volume fraction of entrained primary jet fluid is accompanied by a reduction in the magnitude of the suction force near the edge of the primary jet and, as shown in figure 17, is also accompanied by a reduction in the magnitude of the vectoring force. It should also be noted that when the synthetic jet issues into a co-flowing stream, the location of the stagnation point is influenced by the characteristic advection wavelength of the jet vortices in the co-flow (in the present work this wavelength scales with U_{ave}/f). The downstream migration of the stagnation point suggests that when L_0 is increased, a longer step is necessary to maintain the low-pressure domain.

The data of Smith (1999) show that the normalized time-averaged volume flow rate of primary jet fluid that is entrained by the synthetic jet $\bar{Q}_p/Q$ (Q is the flow rate of the primary jet) decreases with increasing U_{ave} and that the rate of decrease is larger for lower operating frequencies of the synthetic jet. These data also indicate that for fixed U_{ave} and s/h, $\bar{Q}_p/Q$ increases with synthetic jet frequency, while for fixed U_{ave} and f, $\bar{Q}_p/Q$ increases with s/h. It is noteworthy that $\bar{Q}_p/Q$ does not vanish for $s = 0$

(e.g. for $U_{cl} = 7\,\mathrm{m\,s}^{-1}$ and $f = 1120\,\mathrm{Hz}$, more than half of the synthetic jet flow is drawn from the primary jet when $s = 0$).

The preceding discussion emphasizes the role of the volume fraction of primary jet fluid that is diverted into the synthetic jet during the suction stroke in the vectoring of the primary jet. As shown above (e.g. figure 18), the interaction between the two jets leads to the formation of a closed recirculating flow domain between them in which the static pressure is lower than atmospheric and which extends upstream along the upper surface of the primary jet conduit. This pressure difference results in deflection of primary jet fluid toward the surface of the conduit and along the closed recirculating bubble downstream of the primary jet exit plane. In the absence of other forces, fluid elements of the primary jet continue to be advected downstream along the altered direction. It is noted in reference to §6 that if the operating frequency of the synthetic jet is high enough compared to the characteristic time scale of the vectoring of the primary jet, the low-pressure domain becomes quasi-steady.

The dependence of the dimensional resultant force F_y that is associated with the vectoring of the primary jet fluid on some of the relevant flow parameters is shown in figure 17. Given the preceding discussion, it is argued that in the present flow configuration this force depends primarily on the speed of the primary jet U_{ave}, the suction flow of the synthetic jet (as may be measured by U_0), the characteristic measure of the flow asymmetry into the synthetic jet (as represented by s), and the operating frequency of the synthetic jet f. It may also be argued that the characteristic scales of the primary and control jets, H and h, respectively, as well as kinematic viscosity of the fluid v should also be included. Since F_y balances the pressure distribution that is associated with the turning of the flow near the top surface of the conduit, it may be argued that the turning is a local effect that is only weakly dependent on H (provided H is large enough). In fact, in the investigation of Hammond & Redekopp (1997) the force is produced on a flow partition between two streams of infinite extent. Furthermore, it is also argued that if the orifice width of the synthetic jet is small enough so that the details of the flow near the orifice do not substantially affect the global flow field, the effect of this jet may be represented by a 'global' parameter that reflects its strength (similar to a source or a sink in a two-dimensional potential flow).

In the absence of a global length scale for the flow about the corner of the primary jet conduit, the characteristic length scale is taken to be the wavelength of the interaction domain (e.g. the recirculating bubble) between the jets $\lambda = U_{cl}/f$. Therefore, it is anticipated that the interaction between the jets is primarily influenced by s, f and U_{ave} and on dimensional grounds it is argued that:

$$\frac{F_y}{\rho \lambda U_{ave}^2} = G\left(\frac{s}{\lambda}, \frac{U_0}{U_{ave}}, Re_H\right).$$

Figure 23 shows the variation of the dimensionless force (scaled with U_{ave} and λ) with the dimensionless step size s'/λ where $s' = s + s_0$. The offset, s_0 accounts for the fact that even for $s = 0$ there is a finite flow rate of primary jet fluid into the synthetic jet and therefore a finite force. For the present configuration, $s_0 = 5h$ yields a reasonable collapse of the data shown in figure 17. These data suggest that, at least within the present parameter space, the dimensionless force exerted on the conduit is relatively insensitive to the Reynolds number of the primary jet and to the variations in U_0 (approximately 25%, cf. §2) with the exception of the lowest level of U_0 ($Re_{U_0} = 280$).

The preceding discussion establishes that the unsteady flow created by the synthetic jet and the diversion of some primary jet fluid results in a quasi-steady vectoring of the primary jet (cf. figure 26). Although the synthetic jet suction is evidently crucial
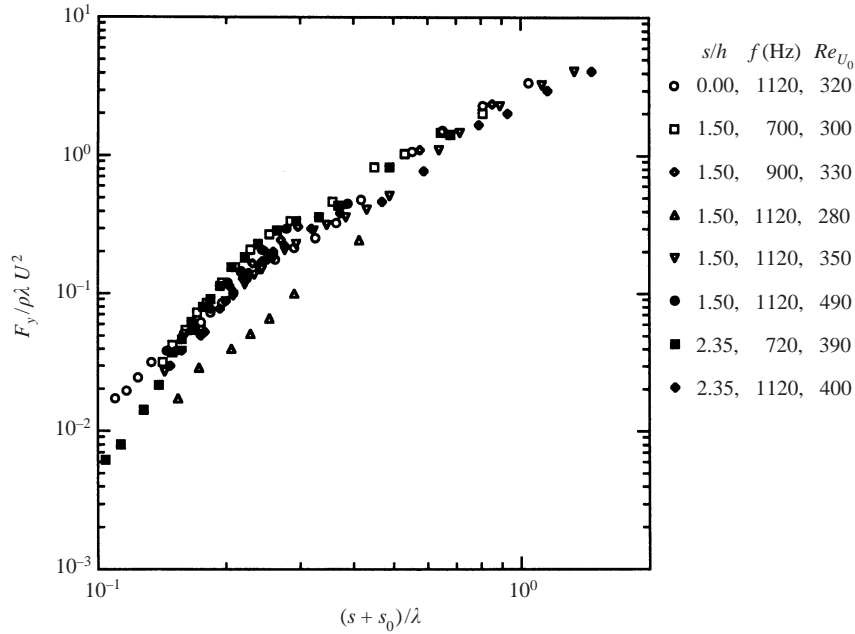
FIGURE 23. Variation of the vectoring force with the dimensionless step size.

to the vectoring effect, it is argued that its streamwise momentum is also critical to vectoring in the absence of an adjacent support surface. It is instructive to consider the replacement of the synthetic jet actuator with steady suction through the same slot. In a laboratory test, it was found that unless the suction flow rate was comparable to that of the primary jet, very little vectoring was achieved. In these experiments, the sink flow is drawn largely from the ambient. A schematic of the flow is shown in figure 24(a). As a result of the suction of a small amount of fluid from the primary jet, a stagnation point (saddle) forms between the sink and the primary jet exit plane. Its location varies with the volume flow rate of the primary jet fluid that can be drawn into the sink. Although the effectiveness of the suction could potentially increase if the lip of the primary jet was rounded, the sink preferentially draws stagnant ambient fluid and therefore has little effect on the primary jet.

The addition of a steady source (or jet) above the sink (figure 24b) places fluid above the sink with significant downstream momentum, and, although some of the source flow is reversed and entrained, more primary jet fluid is entrained than without the source. This flow configuration is directly analogous to the configuration considered in the numerical work of Hammond & Redekopp (1997) in which suction is applied at the downstream end of the flow partition in a shear layer, and results in near-field vectoring. Since the shear layer in that study is infinite in the cross-stream direction, the vectored flow is ultimately turned back to the streamwise direction. In the hypothetical experiment depicted in figure 24(b), the momentum of the source flow can be selected so that the primary jet remains vectored.

6. Characteristic response time of jet vectoring

The actuation discussed in §§ 4 and 5 is applied at frequencies that are typically higher than the 'natural' unstable frequencies of the base flow and therefore, the vectoring of the primary jet may be thought of as quasi-steady. This section discusses
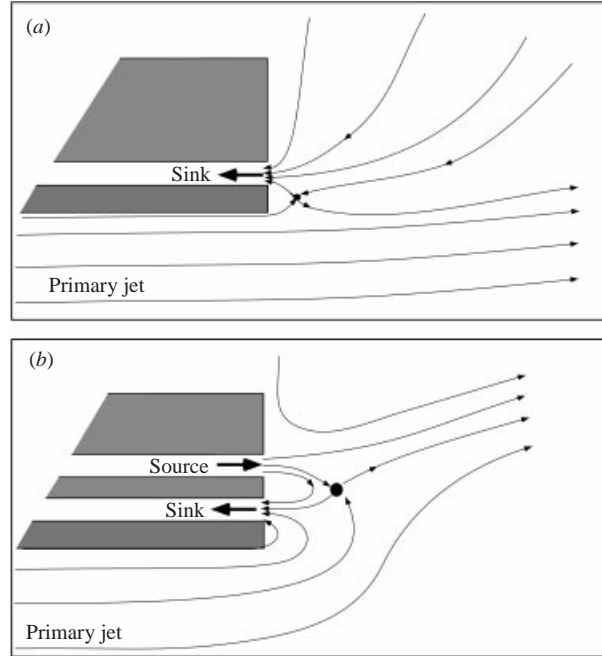
FIGURE 24. Schematic description of the interaction between the primary jet and
(*a*) a two-dimensional sink and (*b*) a source–sink combination.

the characteristic response of the vectored jet to time-varying actuation that is effected using stepped modulation of the actuation driving signal. The time history of the synthetic jet orifice velocity is shown in figure 25 ($f = 1120\,\text{Hz}$ and $s/h = 1.5$). The measurements are taken using a single hot-wire sensor placed at the centre of the jet orifice at midspan, and the rectification of the measured velocity traces is removed. These data show that the amplitude of the velocity within the orifice of the synthetic jet reaches 85% of its final value within two actuator cycles which is indicative of the actuator's response time.

Time traces of the angle of the velocity vector on the centreline of the vectored primary jet are computed from two-component (×-wire) anemometry data at the exit plane and are shown in figure 26 for $U_{cl} = 7$ and $15\,\text{m\,s}^{-1}$. The vectoring angle oscillates at the actuation frequency and its cycle-averaged value increases monotonically and reaches a final level within approximately ten actuation cycles. The nominal amplitudes of the angle oscillations are 3.5° and 3.0° for $U_{cl} = 7\,\text{m\,s}^{-1}$ and $15\,\text{m\,s}^{-1}$, respectively. While at $U_{cl} = 7\,\text{m\,s}^{-1}$, the angle fluctuations are time-harmonic, at $U_{cl} = 15\,\text{m\,s}^{-1}$, the flow within the jet conduit is turbulent, and therefore the angle oscillations include higher-frequency components that are also present before the step modulation is applied. The time variation of the vectoring angle is measured at primary jet centreline velocities ranging from 5 to $20\,\text{m\,s}^{-1}$, and the corresponding characteristic vectoring time, τ_v, is determined using an exponential least-squares fit to the data. The time constant and the final cycle-averaged vectoring angle at each primary jet speed are plotted in figure 27. These data show that the characteristic vectoring time of the primary jet decreases almost linearly with the primary jet speed, and at the upper end of the velocity range, it is approximately two periods of the synthetic jet. The mean vectoring angle at the exit plane also decreases
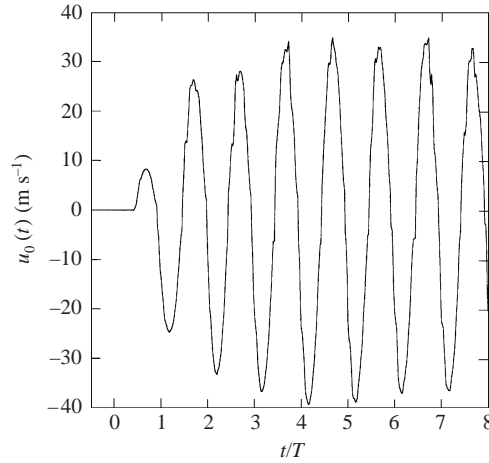
FIGURE 25. The orifice velocity of a step-modulated (beginning at $t/T = 0$) synthetic jet.
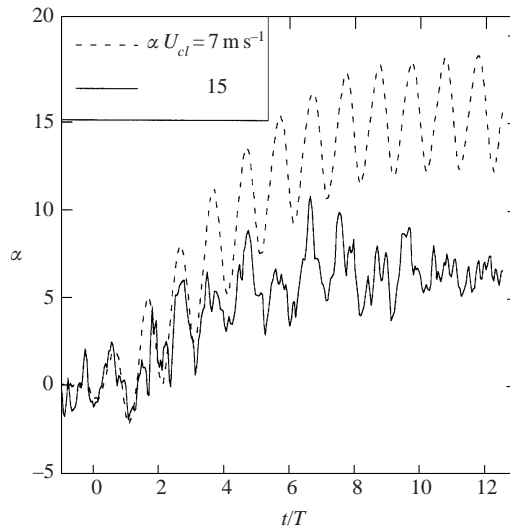
FIGURE 26. Time variation of the angle of the velocity vector on the centreline of the primary jet at the exit plane. The synthetic jet is step modulated at $t/T = 0$.

monotonically with primary jet speed, although the rate of change decreases when the conduit flow becomes turbulent.

The effect of time-periodic modulation of the actuator driving signal (cf. Wiltse & Glezer 1993) is investigated using schlieren visualization. The field of view has a diameter of $11H$ and includes the primary jet exit plane. Both the driving carrier and the modulating waveforms are sinusoidal (the carrier frequency is 1120 Hz, the Reynolds number of the synthetic jet in the absence of modulation is 363, and $s/h = 1.5$).

In figure 28, the effect of amplitude modulation at $f_M = 10$ Hz (i.e. $T_M/\tau_v = 45$) is shown in a sequence of video images that are taken phase-locked to the modulation waveform at six equal increments of the modulation cycle ($U_{cl} = 7$ m s^{-1}, $\tau_v/T = 2.5$). At $t/T_M = 0$ (figure 28a) the primary jet appears to be nearly unforced (vortices
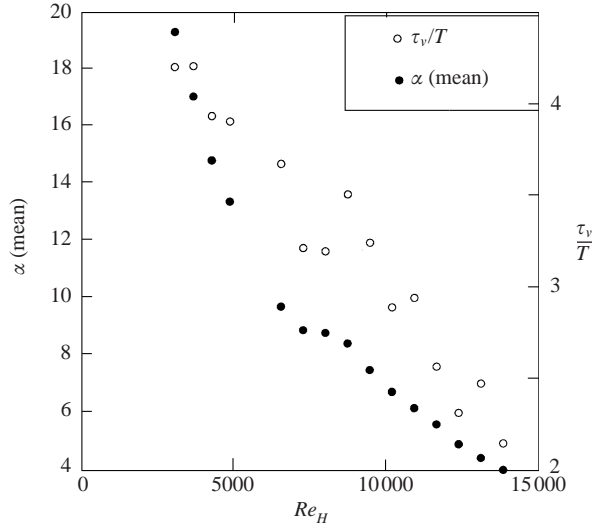
FIGURE 27. The variation with Re_H of the cycle-averaged final vectoring angle and characteristic response time of the primary jet.

at the frequency of the K-H instability are present on both sides of the jet) but is vectored slightly away from the actuator. As the modulation cycle proceeds, the vectoring angle of the primary jet increases, and the vortices within the forced (top) shear layer are no longer present and are replaced by small-scale motions. Of particular note is a vortical structure resembling a starting vortex that forms at the centre of the image in figures 28(b) and 28(c) as the jet approaches its maximum vectoring angle (approximately 30°, as with a non-modulated actuation waveform). The clockwise vortex at the centre of the image in figure 28(b) increases in size and becomes turbulent as it is advected downstream (figure 28c). This vortex appears to entrain the ambient fluid into the jet and its cross-section almost fills the entire height of the image on the right-hand side of figure 28(d). As the modulation cycle passes through $t/T_M = \frac{1}{2}$ (figure 28d), the flow angle of the fluid in the far-field of the jet ($x/H = 5$) is nominally 34°, which is larger that the mean angle in the absence of modulation. At the same time, the vectoring angle of the fluid in the near field of the jet ($x/H \sim 2$) begins to decrease. By $t/T_M = \frac{5}{6}$, the primary jet at, $x/H < 4$ is almost horizontal, although there is a slight overshoot away from the actuator.

When the modulation period is decreased (but is still much longer than the vectoring response time of the primary jet), the streamwise wavelength of the CCW vertical structures described above becomes shorter, as shown in figure 29(a) ($f_M = 60$ Hz, $t/T_M = 0.25$, $T_M/\tau_v = 6.67$). In figure 29(b), the modulation frequency is increased to 120 Hz, which is close to the K-H frequency of the shear layer of the unforced jet (as discussed in connection with figure 11). It is clear that, at this modulation period, the influence of the synthetic jet is greatly reduced, which may be attributed to two simultaneous effects. As shown in figure 25, following a step-modulated input, the synthetic jet reaches a significant fraction of the maximum orifice velocity after only two cycles. In figure 29, the modulating waveform is sinusoidal and therefore the delay associated with the start-up of the jet actuator is somewhat longer, resulting in a significant decrease in the actuation duty cycle which decreases further with increasing modulation frequency. It is plausible that as a result of the reduction in
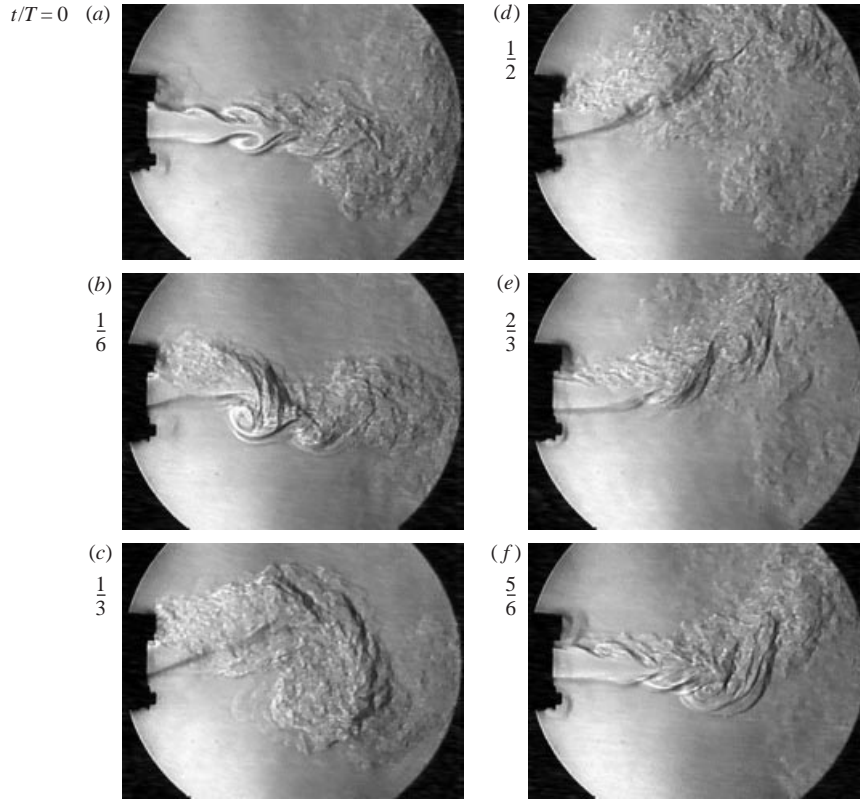
$t/T = 0$ (*a*)

(*d*) $\frac{1}{2}$

(*b*) $\frac{1}{6}$

(*e*) $\frac{2}{3}$

(*c*) $\frac{1}{3}$

(*f*) $\frac{5}{6}$

FIGURE 28. Schieren images of the primary jet forced using amplitude modulated actuation at six equally spaced intervals during the modulation period T_M. The carrier frequency is 1120 Hz and the modulation frequency is 10 Hz.

the duty cycle and consequently in the synthetic jet effectiveness, the K-H instability is not completely suppressed, as is evidenced by the roll-up of vortices within the lower (unforced) shear layer and less coherent vortices in the upper shear layer. (The simulations of Hammond & Redekopp (1997) showed that the presence of the shear-layer instability results in reduced vectoring.) When the modulation frequency is increased to 180 Hz (figure 29c), the mean vectoring angle is reduced compared to the non-modulated case in figure 7, since owing to the modulation, the effective Reynolds number of the synthetic jet averaged over the modulation cycle is reduced by $2/\pi$.

7. Summary and conclusions

The interaction between a primary conventional rectangular air jet and a smaller-scale co-flowing high-aspect-ratio synthetic jet actuator is investigated experimentally. The entrainment of primary jet fluid by the adjacent synthetic jet leads to alteration of the static pressure near the flow boundary and results in deflection of the primary jet toward the synthetic jet even in the absence of an extended control surface (e.g. a diffuser or collar) that is balanced by a force on the primary jet conduit. For a synthetic jet of a given Reynolds number Re_{U_0} and duty cycle and fixed primary jet
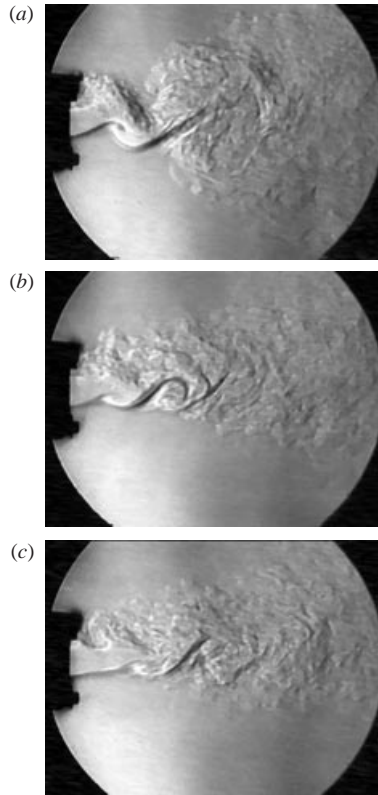
(*a*)

(*b*)

(*c*)

FIGURE 29. Schieren images of the primary jet forced using amplitude modulated actuation. The carrier frequency is 1120 Hz and the modulation frequencies are (*a*) 60 Hz, (*b*) 120 Hz, and (*c*) 180 Hz. The images are aquired at $t/T_M = 0.25$ (T_M is the period of the modulating waveform).

speed, the volume flow rate of primary jet fluid that is diverted into the synthetic jet depends on the driving frequency and, as discussed below, can be regulated by restricting the flow of entrained ambient fluid.

Measurements of the phase-averaged flow in the near field of the synthetic jet demonstrate the disparity between the blowing and suction strokes of the jet. While the nominally two-dimensional flow during the suction stroke is similar to the flow induced by a two-dimensional sink that is coincident with the jet orifice, the flow during the blowing stroke is jet-like and is confined to a finite pie-slice sector that is symmetric about the jet centreline. It is shown that the time-periodic reversal in flow direction along the jet centreline (between the blowing and suction strokes) leads to the formation of a stagnation point on the centreline (downstream of the orifice) whose streamwise position increases with the dimensionless stroke length. The flow into the synthetic jet during the suction stroke is typically restricted to a narrow domain that is bounded by the exit plane of the jet and branches of the stagnation streamline that are nominally parallel to the exit plane and separate between the flow induced during the previous ejection stroke and the flow associated with the suction stroke.

An important finding of the present work is that the symmetry of the suction flow about the jet centreline can be regulated effectively by extending one of the edges of the synthetic jet orifice in the downstream direction. The presence of the extension

(or step in the orifice) restricts the suction flow on that side of the jet centreline and therefore leads to an increase in the flow rate on the opposite side of the jet orifice.

A stagnation point also appears within the interaction domain between the primary jet and the co-flowing synthetic jet. This stagnation point is formed during the suction stroke of the synthetic jet and moves away from the synthetic jet in the downstream direction. The stagnation streamlines divide the flow near the synthetic jet into four quadrants: primary jet fluid that is drawn into the actuator; primary jet fluid which continues to move in the downstream direction; ambient fluid that is drawn into the synthetic jet; and ambient fluid that is advected along the primary jet. The interaction domain includes a closed recirculating flow region in which the static pressure is lower than atmospheric. When the actuation frequency is high enough compared to a characteristic relaxation time of the jet–jet interaction, the low-pressure domain becomes virtually time-independent.

The pressure field that results from the interaction between the two jets and leads to the turning of the primary flow is measurable as far as $2H$ upstream of the exit plane (although most of the contribution to the vectoring force occurs within one jet width of the exit plane). Consequently, the turning of the primary jet flow begins within the flow conduit and the change in the flow direction is nearly complete at the exit plane. The vectoring force increases with primary jet speed and, in most cases, reaches a maximum before it begins to decrease. The primary jet speed at which the vectoring force peaks increases with step size and the actuation frequency. An increase in the strength of the synthetic jet (as may be measured by Re_{U_0}) results in an increase in the vectoring force. For the purpose of scaling of the vectoring force, it is argued that, to lowest order, this force depends primarily on the average speed of the primary jet, the 'global' strength of the sink-like suction flow into the synthetic jet (that is related Re_{U_0}), the flow asymmetry into the synthetic jet (as represented by the step size), and the operating frequency of the synthetic jet. It is also argued that since the interaction between the jets is primarily confined to a domain that is much smaller than the characteristic dimension (width) of the primary jet, the latter does not play a major role in the scaling of the vectoring force. In the absence of a global length scale for the flow about the corner of the primary jet conduit, the characteristic length scale is taken to be the wavelength of the interaction domain (e.g. the recirculating bubble) between the jets. The present data indicate that at least within the present parameter space, the dimensionless force exerted on the conduit depends primarily on the dimensionless step size and is relatively insensitive to variations in the Reynolds number of the synthetic jet.

Finally, the characteristic response time of the primary jet to vectoring effected by an adjacent synthetic jet is investigated using stepped modulation of the driving signal. It is shown that the magnitude of the velocity within the orifice of the synthetic jet reaches about 85% of its final value within two actuation cycles. As the stepped modulation is applied, the imposed vectoring angle oscillates at the actuation frequency and its cycle-averaged value increases monotonically and reaches a final level within ten actuation cycles. Following the transient, the vectoring angle continues to oscillate at the actuation frequency with amplitude that is a relatively small fraction of a non-zero mean. The vectoring time of the primary jet decreases almost linearly with the primary jet speed and at large speeds, it is equal to approximately two periods of the actuation waveform. The mean vectoring angle at the exit plane also decreases monotonically with primary jet speed, although the rate of change decreases when the conduit flow becomes turbulent.

REFERENCES

ADRIAN, R. 1991 Particle imaging techniques for experimental fluid mechanics. *Annu. Rev. Fluid Mech.* **23**, 261–304.

AMITAY, M., SMITH, B. L. & GLEZER, A. 1998 Aerodynamic flow control using synthetic jet technology. *AIAA Paper* 98-0208.

BREMHORST, K. & HOLLIS, P. G. 1990 Velocity field of an axisymmetric pulsed, subsonic air jet. *AIAA J.* **28**, 2043–2049.

COHEN, J. & WYGNANSKI, I. 1987a Evolution of instabilities in the axisymmetric jet. Part 1. The linear growth of disturbances near the nozzle. *J. Fluid Mech.* **176**, 191–219.

COHEN, J. & WYGNANSKI, I. 1987b Evolution of instabilities in the axisymmetric jet. Part 2. The flow resulting from the interaction between two waves. *J. Fluid Mech.* **176**, 221–235.

CROW, S. C. & CHAMPAGNE, F. H. 1971 Orderly structure in jet turbulence. *J. Fluid Mech.* **48**, 547–591.

DIDDEN, N. 1979 On the formation of vortex rings: rolling-up and production of circulation. *Z. angew. Math. Phys.* **30**, 101–116.

FLAMM, J. D. 1998 Experimental study of a nozzle using fluidic counterflow for thrust vectoring. *AIAA Paper* 98-3255.

GLEZER, A. 1998 The formation of vortex rings. *Phys. Fluids* **31**, 3532–3542.

GUTMARK, E. & WYGNANSKI, I. 1976 The planar turbulent jet. *J. Fluid Mech.* **73**, 465–495.

HAMMOND, D. A. & REDEKOPP, L. G. 1997 Global dynamics and aerodynamic flow vectoring of wakes. *J. Fluid Mech.* **338**, 231–248.

JOYCE, J. W. 1983 Fluidics – Basic Component and Applications. Special Rep. HDL-SR-83-9.

KOCH, C. R. 1990 Closed loop control of a round jet/diffuser in transitory stall. PhD thesis, Stanford University.

NEWMAN, B. G. 1961 The deflexion of plane jets by adjacent boundaries – Coanda effect. In *Boundary Layer and Flow Control* (ed. G. V. Lachmann), vol. 1, pp. 232–264.

PACK, L. G. & SEIFERT, A. 1999 Periodic excitation for jet vectoring and enhanced spreading. *AIAA Paper* 99-0672.

RAFFEL, M., WILLERT, C. & KOMPENHANS, J. 1998 *Particle Image Velocimetry*. Springer.

RAMAN, G. & CORNELIUS, D. 1995 Jet mixing control using excitation from miniature oscillating jets. *AIAA J.* **33**, 365–368.

SMITH, B. L. 1999 Synthetic jets and their interaction with adjacent jets. PhD thesis, Georgia Institute of Technology School of Mechanical Engineering.

SMITH, B. L. & GLEZER, A. 1994 Vectoring a high aspect ratio rectangular air jet using a zero-net-mass-flux control jet. *Bull. Am. Phys. Soc.* **39**, 1894.

SMITH, B. L. & GLEZER, A. 1997 Vectoring and small-scale motions effected in free shear flows using synthetic jet actuators. *AIAA Paper* 97-0213.

SMITH, B. L. & GLEZER, A. 1998 The formation and evolution of synthetic jets. *Phys. Fluids* **10**, 2281–2297.

SMITH, B. L. & SWIFT, G. W. 2001 Synthetic jets at large Reynolds number and comparison to continuous jets. *AIAA Paper* 2001–3030.

SMITH, B. L., TRAUTMAN, M. A. & GLEZER, A. 1999 Controlled interactions of adjacent synthetic jets. *AIAA Paper* 99-0669.

STRYKOWSKI, P. J., KROTHAPALLI, A. & FORLITI, D. J. 1996 Counterflow thrust vectoring. *AIAA J.* **34**, 2306–2314.

VIETS, H. 1975 Flip-flop jet nozzle. *AIAA J.* **13**, 1375–1379.

WILTSE, J. M. & GLEZER, A. 1993 Manipulation of free shear flows using piezoelectric actuators. *J. Fluid Mech.* **249**, 261–289.

WILTSE, J. M. & GLEZER, A. 1998 Direct excitation of small-scale motions in free shear flows. *Phys. Fluids* **10**, 2026–2036.